Energy Conversion and Management 370 (2026) 122159

Contents lists available at ScienceDirect

Energy Conversion and Management

journal homepage: www.elsevier.com/locate/enconman

Research Paper

# Techno-economic assessment of hybrid solar spectral-splitting PV–thermal green hydrogen production systems

Yu Tian [a], Pooria Hadikhani [b], Christos N. Markides [c], Gan Huang [a,*]

[a] Institute of Microstructure Technology, Karlsruhe Institute of Technology, Hermann-von-Helmholtz-Platz 1, 76344 Eggenstein-Leopoldshafen, Germany
[b] REMA Hydrogen AG, Lausanne, Switzerland
[c] Clean Energy Processes (CEP) Laboratory, Department of Chemical Engineering, Imperial College London, London SW7 2AZ, UK

A B S T R A C T

This study presents a comprehensive techno-economic assessment of a spectral-splitting photovoltaic-thermal hydrogen system across diverse climatic zones in Karlsruhe, Barcelona, Cairo and Dunhuang. By integrating optical-thermal simulations with an economic model, the analysis quantifies the impact of geography and tracking strategies on techno-economic performance. Results demonstrate a peak annual solar-to-hydrogen efficiency of around 20 % in high-irradiance regions like Cairo; specifically, while Cairo achieved the highest summer production yields, Dunhuang exhibited a unique profile that mitigates seasonal fluctuations, resulting in comparatively uniform hydrogen production throughout the year. The comparative analysis demonstrates that the substantial gain in hydrogen yield from dual axis tracking outweighs the incremental hardware costs. This establishes dual axis tracking as the economic optimum, reducing the levelized cost of hydrogen (LCOH) to 6.0 €/kg, approximately 9.6 % lower than the single axis baseline. Furthermore, Monte Carlo uncertainty analysis confirms that deploying the system in high-irradiance sites significantly compresses investment risk. Under hydrogen-only revenue situations, the discounted payback time (PBT) is around 6 years for dual axis configurations in Cairo and Dunhuang, while commercial valorisation of the oxygen byproduct accelerates capital recovery, reducing the PBT to around 5 years in Cairo.

## 1. Introduction

Hydrogen is widely recognized as a cornerstone of the future zero-carbon energy system, offering a pathway to decarbonize hard-to-abate sectors [1]. Despite its promise, the current production landscape remains dominated by fossil fuels. As of late 2022, nearly 83% of global hydrogen was derived from natural gas and coal without carbon capture, termed 'grey' or 'black' hydrogen, accounting for significant $CO_2$ emissions [2,3]. To align with global sustainability goals, a transition to green hydrogen, produced via water electrolysis powered by renewable energy, is imperative [4]. However, economic competitiveness remains the primary barrier to widespread adoption. Current green hydrogen costs, typically ranging from €3 to €8 per kilogram, are significantly higher than fossil-based alternatives of €1 to €2 per kilogram [5]. Major global initiatives, such as the U.S. Department of Energy's "Hydrogen Shot," have set ambitious targets to reduce the cost to $1/kg within a decade [6]. Achieving this goal requires not just incremental cost reductions in components, but disruptive technological innovations that can drastically boost solar-to-hydrogen (STH) conversion efficiency to offset system costs [7,8].

Among various renewable pathways, solar photovoltaic (PV) driven electrolysis has emerged as a frontrunner due to the plummeting costs of commercial PV modules [9,10]. However, standard PV-electrolysis (PV-EC) systems face a fundamental thermodynamic limitation: they typically utilize only the short wavelength portion of the solar spectrum for electricity generation, while the infrared spectrum is either wasted or, worse, converted into waste heat that degrades PV performance [11,12]. While concentrated PV (CPV) concepts coupled with high-efficiency multijunction cells have demonstrated high STH efficiencies in laboratory settings [13,14] and have even been realized in kW-scale prototypes [15], the associated thermal management remains a critical engineering challenge. In parallel, the operating temperature limitations of commercial low-temperature electrolyzers constitute a significant bottleneck for STH efficiency. Conventional proton exchange membrane (PEM), alkaline water electrolyzer (AWE), and anion exchange membrane (AEM) technologies are strictly confined to operating temperatures below 80 °C to maintain membrane stability [16,17]. This thermal constraint prevents the utilization of high-grade solar heat to thermodynamically lower the kinetic overpotentials of the water splitting reaction, thereby precluding the exploitation of thermal-electrical synergy.

To address these limitations, hybrid photovoltaic-thermal (PVT)

* Corresponding author.
*E-mail address:* gan.huang@kit.edu (G. Huang).

https://doi.org/10.1016/j.enconman.2026.122159
Received 22 June 2026; Received in revised form 25 August 2026; Accepted 6 September 2026
Available online 14 September 2026

architectures employing spectral splitting have gained increasing attention in recent years [18,19], including specifically for hydrogen production [20,21]. By optically decoupling the solar spectrum, these systems direct short wavelengths to PV cells and long wavelengths to thermal absorbers, enabling simultaneous high-efficiency power generation and high-temperature heat collection. Most PVT collectors are designed for low-grade heat or hot water provision, either directly [22] or via the use of heat pumps [23]. Here, extending upon this concept, in our recent work [24], we designed and experimentally validated a spectral-splitting photovoltaic-thermal hydrogen (SSPVTH) system. By integrating emerging membrane-less electrolyzers, which tolerate significantly higher temperatures than PEM, AEM, and AWE cells (*e.g.*, [25]), the system effectively utilizes high-grade solar heat to reduce the electrolysis activation barrier [26,27]. This design achieved a peak STH efficiency of 21.1% with GaAs cells, demonstrating a clear physical advantage over standalone PV-EC systems [24].

While the thermodynamic superiority of such hybrid concentrated systems is evident, their economic viability under realistic operating conditions remains a critical open question. Most existing studies have primarily focused on performance optimization under standard steady-state Air Mass 1.5 (AM1.5) irradiance, often overlooking the economic trade-offs of increased system complexity. The SSPVTH architecture introduces additional hardware compared to standard flat-panel PV systems, including parabolic concentrators, spectral-splitting filters, and

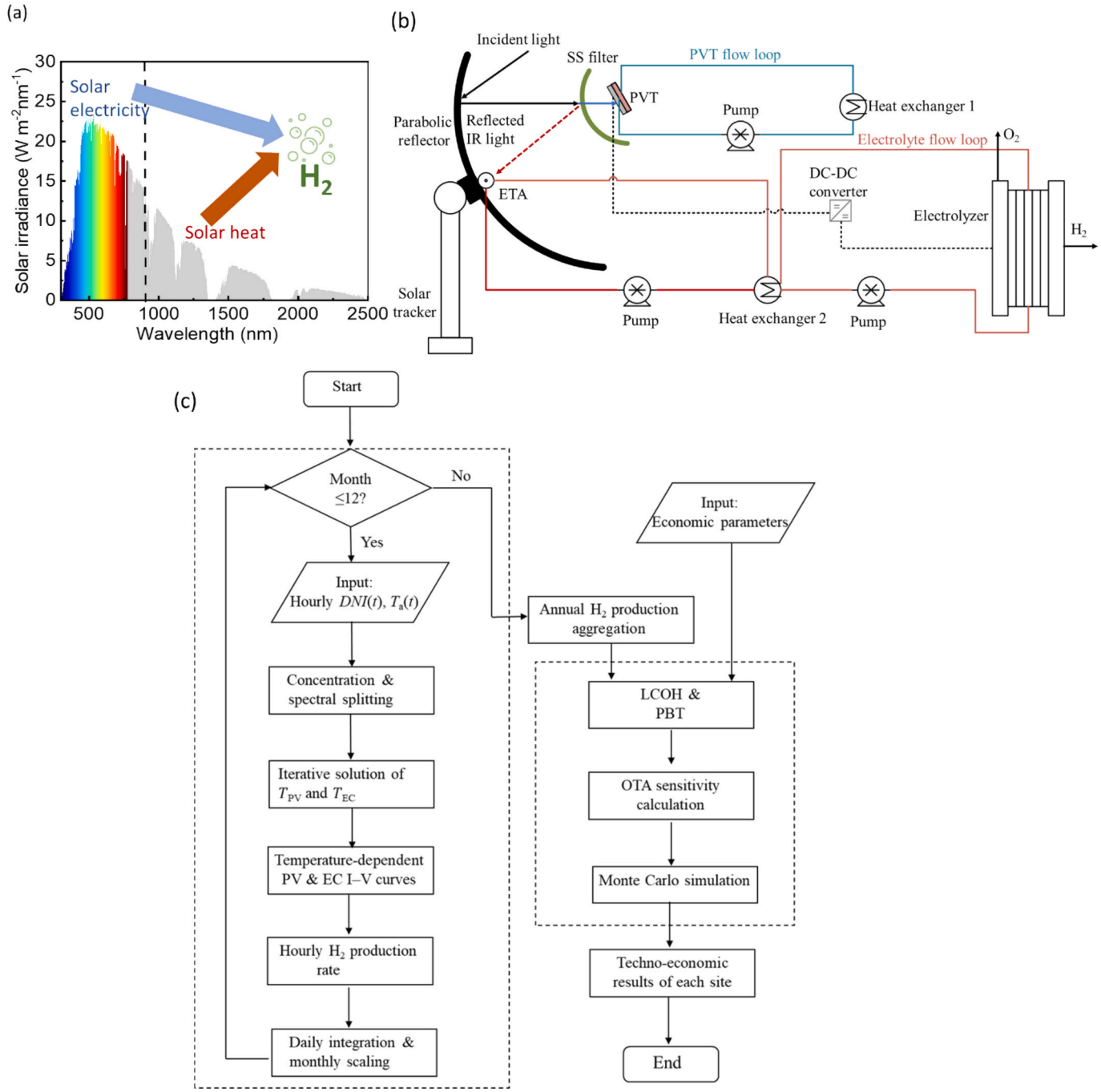


**Fig. 1.** Diagrams of hybrid solar spectral-splitting PV–thermal green hydrogen production systems and the techno-economic assessment framework. (a) Concept of spectral-splitting PV–thermal green hydrogen production. (b) Schematic diagram of the SSPVTH system. (c) Flowchart of the techno-economic assessment framework.

dual-loop thermal management components. Moreover, high optical concentration typically requires precise dual axis tracking, which significantly increases the initial capital expenditure (CAPEX) [28,29]. Consequently, a fundamental techno-economic tension exists regarding whether the enhanced hydrogen yield derived from high-efficiency spectral splitting is sufficient to economically justify the increased CAPEX. Furthermore, the stability of this cost-benefit balance under the highly dynamic fluctuations of real-world solar irradiance and ambient temperatures, as opposed to static laboratory conditions, remains to be rigorously quantified. Therefore, static performance metrics are insufficient to capture the true economic potential, and a rigorous techno-economic assessment across diverse geographical latitudes is urgently needed [30,31].

To bridge this gap, this study presents a comprehensive techno-economic assessment of the hybrid SSPVTH solar system. Unlike previous studies that focused solely on efficiency under standard laboratory test conditions, this work integrates a rigorous simulation considering real-world transient meteorological data with a discounted cash flow (DCF) model to evaluate the system's commercial potential. The specific objectives are: (i) to assess the system's geographical adaptability across four distinct climatic zones identifying the “sweet spots” for deployment; (ii) to optimize the tracking strategy by rigorously comparing the trade-offs between high-precision dual axis tracking and lower-cost single axis tracking, determining whether the high yields can justify higher CAPEX; and (iii) to evaluate commercial viability and risk by calculating the levelized cost of hydrogen (LCOH) and discounted payback time (PBT), while quantifying investment risks under market sensitivity and uncertainty.

## 2. System description

### 2.1. Spectral-splitting photovoltaic-thermal hydrogen system concepts

This study investigates a hybrid SSPVTH solar system designed to maximize the utilization of the full solar spectrum for green hydrogen production. Building upon our previous proof-of-concept work [24], as shown in Fig. 1**(a)**, the incident AM 1.5 solar spectrum is divided at a cut-off wavelength, where the higher-energy photons are utilized for photovoltaic electricity generation, while the longer-wavelength infrared portion is redirected for solar thermal harvesting. Instead of dissipating sub-bandgap photons as heat within the PV, this spectral partitioning strategy enables parallel electrical and thermal energy pathways that jointly contribute to hydrogen production. The system layout is schematically illustrated in Fig. 1**(b).** The core of the system is a concentrated PVT (CPVT) system with a parabolic trough concentrator that focuses incident sunlight onto a spectral-splitting (SS) optical filter. This filter acts as a spectral beam splitter, dividing the solar spectrum into two distinct bands based on a specific cut-off wavelength. Photons with wavelengths shorter than cutting edge (cut-off wavelength) are transmitted to the PV module for electricity generation, while longer-wavelength photons are reflected onto an evacuated tube absorber (ETA) to generate high-grade thermal energy. This decoupled optical management ensures that the PV cells operate within their optimal spectral response range while simultaneously harvesting the infrared spectrum as usable heat.

A distinct feature of the proposed system is its dual-loop thermal management strategy, designed to synergize the electrical and thermal outputs. As shown in the PVT flow loop of Fig. 1**(b)**, a low-temperature cooling circuit actively removes waste heat from the PV module, maintaining cell efficiency via Heat Exchanger 1 (HX1). In parallel, the red loop circulates a heat transfer fluid (HTF) through the ETA to capture high-temperature heat. Unlike conventional PVT systems, this high-grade heat is not merely a byproduct but is actively coupled to the hydrogen production unit via Heat Exchanger 2 (HX2). The HTF heats the electrolyte before it enters the electrolyzer stack, thereby thermodynamically lowering the required overpotential for water splitting.

Another distinct feature of the SSPVTH system is the employment of a membrane-less electrolyzer stack [26,27], selected for its superior performance at elevated operating temperatures compared to conventional membrane-based counterparts. The electrolyzer stack comprises multiple cells connected in series and parallel configurations to match the voltage and current characteristics of the PV module. To further enhance system robustness against solar intermittency, a direct current to direct current (DC-DC) converter is integrated between the PV module and the electrolyzer. This power electronic interface regulates the operating voltage, ensuring that the electrolyzer operates near the maximum power point (MPP) of the PV array under varying irradiance conditions. This electro-thermal coupling architecture enables the system to produce hydrogen with enhanced STH efficiency compared to stand-alone PV-electrolyzer systems.

For all geographical sites evaluated in this study, the system operating conditions are set to the optimal values established in our previous detailed analysis [24]. These parameters include an optimal optical concentration ratio of 20×, the flow rate of the HTF and electrolyte, the specific cut-off wavelength of the spectral filter, and the series-parallel configuration of the electrolyzer stack.

To evaluate the feasibility of the proposed design, a comprehensive techno-economic assessment framework was developed, as illustrated in the computational flowchart in Fig. 1**(c)**. The simulation workflow follows a sequential two-phase structure. The first phase focuses on the technical system simulation. It employs a nested temporal loop comprising twelve monthly average daily profiles and hourly time steps to capture the dynamic response of the system under varying meteorological conditions. A core feature of this phase is the coupled thermal-electrical solver, which iteratively determines the equilibrium temperatures of the PV module and the electrolyzer. This ensures that the temperature-dependent electrical characteristics and electrochemical overpotentials are accurately resolved before calculating the hourly hydrogen production rate. The second phase handles the economic assessment. The aggregated annual hydrogen yield from the physical model serves as the primary input, combined with market-based economic parameters, to compute key financial indicators such as the LCOH and PBT. Finally, the framework incorporates a sensitivity analysis and a Monte Carlo simulation to quantify investment risks and system robustness against market uncertainties.

### 2.2. Case study locations and climatic conditions

To comprehensively evaluate the techno economic feasibility of the proposed SSPVTH system under varying geographical and climatic constraints, four representative sites were selected for this study: Karlsruhe (Germany), Barcelona (Spain), Cairo (Egypt), and Dunhuang (China). These locations were chosen to cover a diverse spectrum of solar resource profiles, ranging from low-irradiance temperate zones to high-irradiance arid desert environments, thereby testing the system's adaptability and economic limits. The meteorological data for these sites, including global horizontal irradiance (GHI), direct normal irradiance (DNI), and ambient temperature, were retrieved from the Photovoltaic Geographical Information System (PVGIS) solar radiation database [32]. To efficiently simulate annual performance while capturing diurnal dynamics, the monthly average daily profile method was adopted. For each calendar month, a synthetic 24-hour profile of solar irradiance and ambient temperature was obtained from the PVGIS daily radiation tool. Each hourly value represents the average of the corresponding hour over all days of that month across the available multi-year period. The system was simulated hourly using these twelve monthly average daily profiles. The resulting hourly outputs were integrated to obtain daily totals and then multiplied by the number of days in the corresponding month to derive the monthly and annual values.

To evaluate the influence of temporal resolution on the predicted technical performance, an independent 8760-hour typical meteorological year (TMY) dataset was also obtained from PVGIS for each study site

[32]. The PVGIS TMY is a synthetic annual meteorological time series assembled from twelve statistically typical calendar months selected from the available multi-year record. Consequently, the individual months may originate from different historical years, but together they form a continuous January-to-December sequence containing 8760 hourly records. Unlike the monthly average daily profile method, which represents each month using an averaged 24-hour profile, the TMY data retain the hour-to-hour and day-to-day meteorological variability within the selected months. The hourly DNI and ambient temperature from the hourly TMY method datasets were supplied to the same SSPVTH simulation model using identical system parameters, tracking models, and the same minimum operating irradiance threshold. The hourly TMY method simulations were used solely to assess the technical performance and annual hydrogen production and were not included in the economic analysis.

Aggregated monthly totals of solar irradiance and average ambient temperatures are shown in Fig. 2. A critical distinction is made between GHI and DNI, as the proposed system utilizes a parabolic reflector that relies exclusively on direct beam radiation. The data reveal a significant disparity in resource quality across the latitudes. High-potential regions, specifically Cairo and Dunhuang, exhibit exceptional solar resources with consistently high radiation levels throughout the year. In contrast, Karlsruhe displays marked seasonality, with a distinct decline in irradiance during winter months. As further shown in Fig. 2, the GHI values follow the expected gradual seasonal trend, indicating that the distinctive DNI variations are not caused by the data-processing procedure. The lower DNI in Barcelona in June is associated with a higher diffuse-radiation contribution, whereas the higher DNI in Dunhuang in March indicates a larger direct-beam fraction and clearer atmospheric conditions. These variations originate from the monthly average profiles in the PVGIS-ERA5 dataset and directly affect the monthly performance of the DNI-dependent SSPVTH system.

The detailed average hourly profiles of irradiance and temperature in July are shown in Fig. 3, serving as an example of the input data used for the hourly simulation. To accurately simulate the operational conditions of the proposed system, the irradiance data in Fig. 3 were extracted for a dual axis solar-tracking plane. It is important to note that for the concentrating optical system, the direct component constitutes the sole effective energy input utilized by the parabolic reflector. For the dual axis tracking configuration, the DNI serves directly as this energy input. However, for the single axis tracking system, the DNI cannot be utilized directly; instead, the incidence angle between the receiving surface and the solar rays must be accounted for. This geometric conversion process is detailed in Section 3.1.

To facilitate a direct comparison between the winter and summer operating conditions, Fig. 4 presents the monthly average hourly irradiance and ambient temperature profiles in January for the same four study sites, corresponding to the July profiles shown in Fig. 3.

## 3. Methodology

The energy conversion process of the solar hydrogen systems in this study is simulated using in-house codes based on principles of energy balance and thermodynamics. The governing equations for various models are detailed below.

### 3.1. Solar irradiance and solar tracking models

Hourly DNI was used as the primary solar resource input in this study. DNI represents the direct beam solar irradiance incident on a

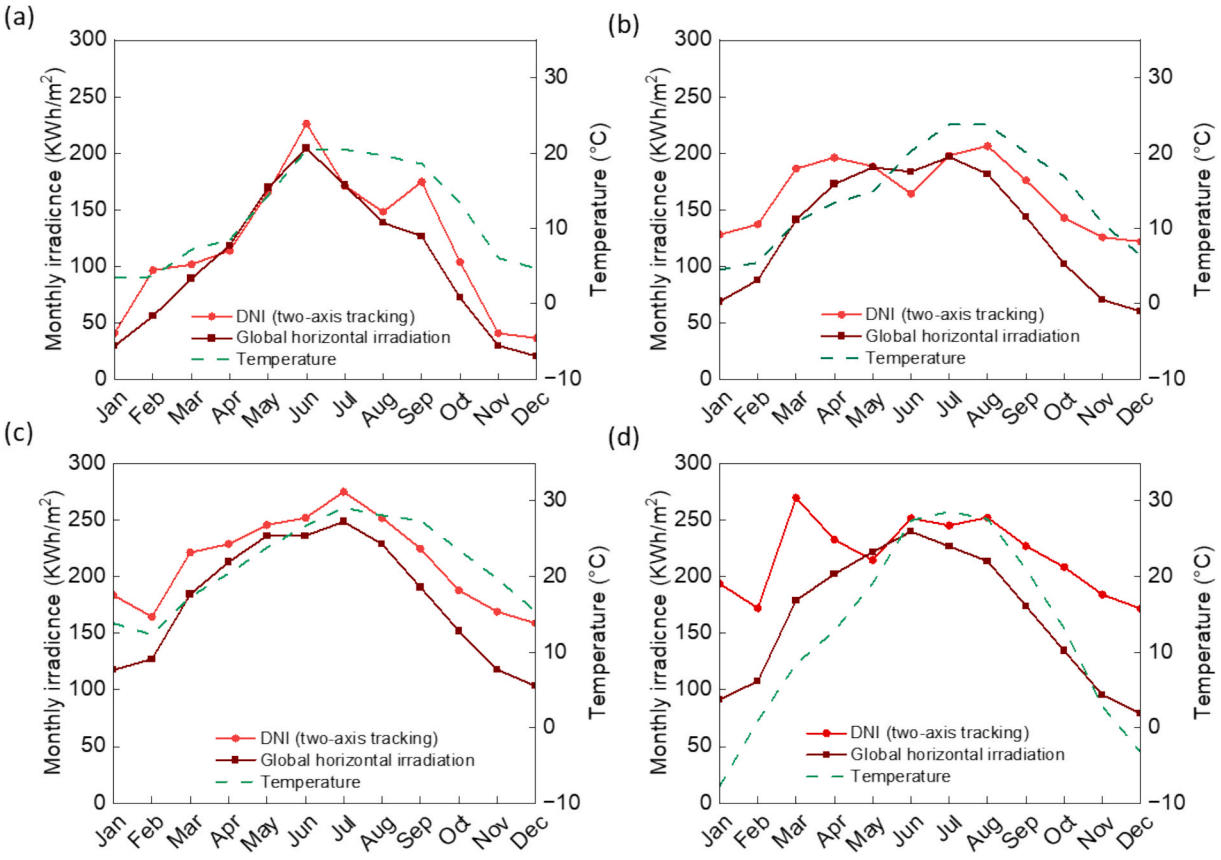


**Fig. 2.** Monthly meteorological data for the selected study sites: (a) Karlsruhe, Germany; (b) Barcelona, Spain; (c) Cairo, Egypt; and (d) Dunhuang, China. The plots show monthly totals for global horizontal irradiance (GHI) and DNI, alongside the average ambient temperature. Data was obtained from the PVGIS solar radiation database [32].

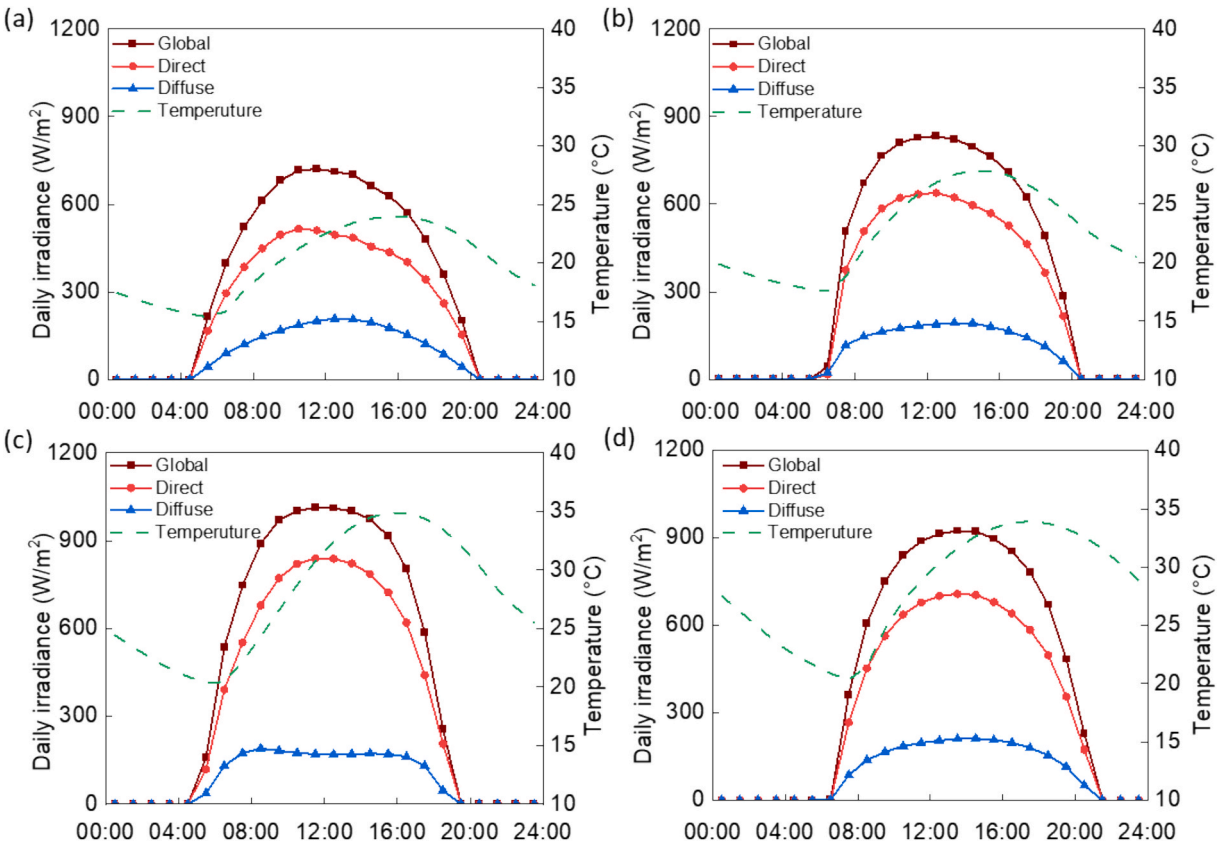


**Fig. 3.** Diurnal profiles of average solar irradiance and ambient temperature distributions in July at the reference sites: (a) Karlsruhe, (b) Barcelona, (c) Cairo, and (d) Dunhuang. The data represents the irradiance received on a dual axis solar tracking plane, comprising global irradiance (global), direct normal irradiance (direct), and diffuse irradiance (diffuse). The ambient temperature variation is shown on the secondary axis.

surface that is continuously oriented normally to the sun and therefore corresponds to an ideal dual axis tracking (DA) reference. To enable a consistent comparison between dual axis and single axis tracking (SA) configurations, the hourly DNI data were converted into an effective beam irradiance incident on a single axis collector aperture using a geometric projection approach based on solar position calculations.

Hourly DNI and ambient air temperature data Ta($t$) were obtained from the PVGIS provided by the European Commission Joint Research Centre (JRC) [32]. To evaluate the annual system performance, monthly average hourly profiles were utilized. For each calendar month, an average daily profile is constructed by averaging the solar irradiance for each hour of the day across all days in that month over the available multi-year historical record. This methodology inherently accounts for the stochastic variations in weather and cloud cover. The monthly aggregate performance is subsequently derived by integrating these averaged hourly profiles and scaling the result by the number of days in the respective month. All angular quantities in this section are expressed in degrees, and all trigonometric functions are evaluated accordingly.

### 3.1.1. Solar position calculation

The solar position is characterised by the solar elevation angle $\alpha$ and solar azimuth angle $\gamma_s$, which together define the direction of the incoming direct solar beam. These angles are calculated as functions of geographical location and time. The local solar time (*LST*) is then calculated as:

$$LST = t + \frac{TC}{60} \tag{1}$$

and the daylight-saving time is not considered. The time correction (*TC*), expressed in minutes, accounts for both the longitude difference between the site longitude $\lambda$ and the local standard time meridian (*LSTM*), as well as the equation of time (*EoT*):

$$TC = 4(\lambda - LSTM) + EoT \tag{2}$$

To convert the local clock time $t$ into local *LST*, a longitude-based time correction is applied. The time zone (*TZ*) denotes the local time zone offset relative to Coordinated Universal Time (UTC), expressed in hours. The corresponding *LSTM* is given by:

$$LSTM = 15 \times TZ \tag{3}$$

and the *EoT* is evaluated as [33]:

$$\mathrm{EoT} = 9.87\sin(2B) - 7.53\cos(B) - 1.5\sin(B) \tag{4}$$

where $B$ is an auxiliary angle depending on the day of year $n$:

$$\mathrm{B} = \frac{360^{\circ}}{365}(n - 81) \tag{5}$$

here, the coefficients 9.87, 7.53 and 1.50 are empirical constants originating from the standard approximation of Earth's orbital eccentricity and axial tilt. The solar elevation angle $\alpha$, representing the angular height of the sun above the local horizon, is obtained from:

$$\alpha = \arcsin(\sin\phi\sin\delta + \cos\phi\cos\delta\cos\omega) \tag{6}$$

where $\phi$ is the site latitude. The solar declination angle $\delta$, defined as the angular position of the sun relative to the Earth's equatorial plane, is evaluated from [33]:

$$\delta = 23.45\sin\left(\frac{360(284+n)}{365}\right) \tag{7}$$

where 23.45° corresponds to the Earth's axial tilt, and the hour angle $\omega$,

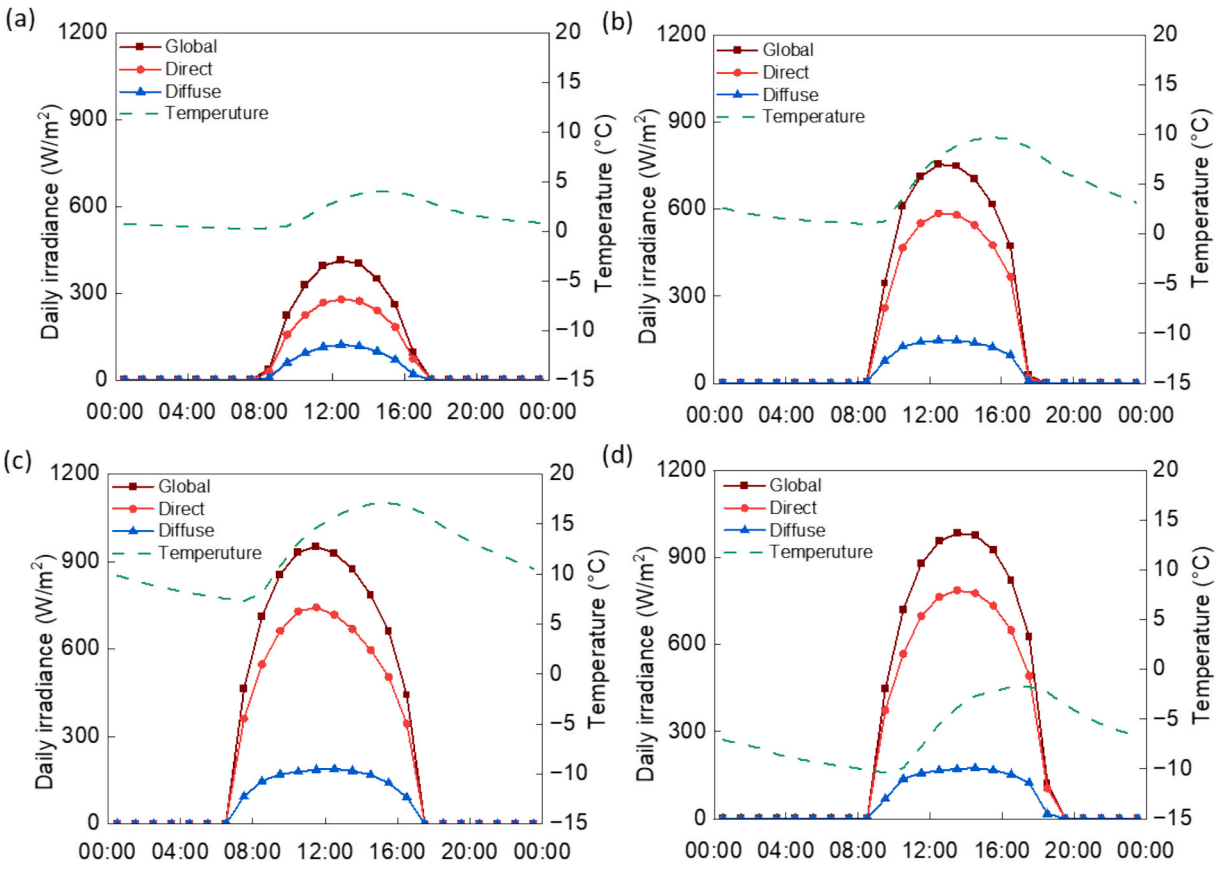


**Fig. 4.** Diurnal profiles of average solar irradiance and ambient temperature distributions in January at the reference sites: (a) Karlsruhe, (b) Barcelona, (c) Cairo, and (d) Dunhuang. The data represents the irradiance received on a dual axis solar tracking plane, comprising global irradiance (global), direct normal irradiance (direct), and diffuse irradiance (diffuse). The ambient temperature variation is shown on the secondary axis.

which represents the angular displacement of the sun from the local meridian from:

$$\omega = 15(LST - 12) \tag{8}$$

The solar azimuth angle $\gamma_s$, describing the horizontal direction of the sun, is computed using an atan2-based formulation to preserve the correct quadrant:

$$\sin\gamma_s = -\frac{\cos\delta\sin\omega}{\cos\alpha} \tag{9}$$

$$\cos\gamma_s = \frac{\sin\delta - \sin\alpha\sin\phi}{\cos\alpha\cos\phi} \tag{10}$$

$$\gamma_s = \text{atan2}(\sin\gamma_s, \cos\gamma_s) \tag{11}$$

where $\gamma_s$ is mapped to the range 0 to 360°.

### 3.1.2. Single axis tracking geometry and irradiance projection

To represent a SA configuration with one rotational degree of freedom, the instantaneous orientation of the collector aperture is derived from the solar position and subsequently used to project the DNI onto the aperture plane [33].

The solar direction is characterised by the solar elevation angle α and the solar azimuth angle $\gamma_s$. Based on these angles, an effective rotation angle is defined to describe the aperture orientation that maximizes beam interception under a single axis constraint. The effective beam irradiance incident on the single axis collector aperture is finally obtained by geometrically projecting the direct normal irradiance onto the aperture plane:

$$DNI_{SA}(t) = DNI_{DA}(t)\cos\theta_i \tag{12}$$

where $DNI_{SA}(t)$ represents the physically accessible beam irradiance under single axis tracking conditions. The original $DNI_{DA}(t)$ time series is retained as dual axis tracking reference. The collector aperture is assumed to be south facing, with a fixed collector azimuth angle $\gamma_c$ equal to 180°, corresponding to a conventional reference orientation in the northern hemisphere. Using the signed effective rotation angle $\beta=\theta_{eff}$, the cosine of the incidence angle between the solar beam and the aperture normal is:

$$\cos\theta_i = \sin\alpha\cos\beta + \cos\alpha\sin\beta\cos(\gamma_s - \gamma_c) \tag{13}$$

with negative values of $\cos\theta_i$ corresponding to back-side illumination of the aperture, are physically meaningless and therefore excluded. Since inverse trigonometric functions yield unsigned angles, a sign convention is introduced to distinguish morning and afternoon orientations and to ensure a continuous single axis rotation. The signed effective rotation angle is therefore defined as:

$$\theta_{eff} = \text{sign}(-\cos\alpha\cos\gamma_s)\theta_{eff,u} \tag{14}$$

This sign assignment in Eq. (14) does not affect the magnitude of the projected irradiance but ensures a physically consistent description of the aperture rotation direction over the course of the day. An unsigned effective projection angle is:

$$\theta_{eff,u} = \arccos\left(\frac{\sin\alpha}{\sqrt{(\cos\alpha\cos\gamma_s)^2 + \sin^2\alpha}}\right) \tag{15}$$

where the denominator corresponds to the magnitude of the solar direction vector projected onto the plane orthogonal to the tracking axis. In this formulation, the vertical component of the solar direction vector is given by sin$\alpha$, consistent with the definition of the solar elevation angle. The tracking model assumes ideal positioning within the prescribed single axis and dual axis geometries. End losses are neglected because the collector modules can be connected end-to-end to form sufficiently long continuous rows. Nominal component optical efficiencies are included, whereas field-specific losses associated with row shading, tracking errors, reflector slope errors, receiver misalignment, variations in the interception factor, and wind-stow operation are not explicitly modelled. These effects depend strongly on the specific solar-field layout and operating conditions and should be incorporated in future field-specific assessments.

The resulting irradiance inputs are subsequently used for annual system performance simulations and hydrogen production calculations. Fig. 5 shows the monthly average daily irradiance profiles for the single axis and dual axis configurations in Cairo, Egypt, for July.

### 3.2. System performance model

#### 3.2.1. Light distribution model

To retain the spectral-splitting framework developed in our previous work while enabling hourly simulations, the terrestrial air mass 1.5 direct (AM1.5D) spectrum is adopted as the reference spectral shape. The model assumes that the instantaneous spectral irradiance scales proportionally with the broadband irradiance while maintaining an invariant spectral distribution. First, the total reference irradiance of the AM1.5D spectrum, $S_{\mathrm{AM1.5D}}$, is obtained by integrating the standard AM1.5D spectral irradiance $G_{\mathrm{AM1.5D}}$ over the solar spectrum range:

$$S_{\mathrm{AM1.5D}} = \int_{280\ \mathrm{nm}}^{4000\ \mathrm{nm}} G_{\mathrm{AM1.5D}}(\lambda)\mathrm{d}\lambda \tag{16}$$

Subsequently, a time-dependent scaling factor $\kappa(t)$ is defined as the ratio of the available broadband irradiance to this reference value:

$$\kappa(t) = \frac{S_{\mathrm{real}}(t)}{S_{\mathrm{AM1.5D}}} \tag{17}$$

where $S_{\mathrm{real}}(t)$ represents the effective broadband beam irradiance incident on the collector aperture. For the dual axis tracking baseline, $S_{\mathrm{real}}(t)$ corresponds to the meteorological $DNI_{\mathrm{DA}}$(t), whereas for the single axis tracking configuration, it corresponds to the projected irradiance $DNI_{\mathrm{SA}}$(t). Finally, the time-resolved spectral irradiance at time $t$ is calculated as:

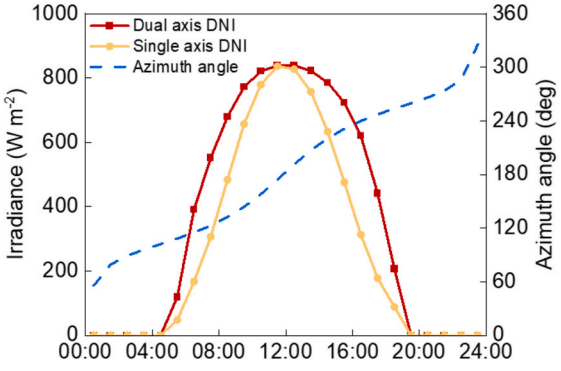


**Fig. 5.** Comparison of the effective solar energy input between the single axis and dual axis tracking strategies using the monthly average daily profile for July in Cairo. The dual axis DNI represents the energy input by the dual axis tracking system. The single axis DNI represents the energy input by the single axis tracking system. The dashed line indicates the variation of the solar azimuth angle, which drives the geometric misalignment in the single axis configurations.

$$G(\lambda, t) = \kappa(t) G_{\mathrm{AM1.5D}}(\lambda) \tag{18}$$

The light is initially concentrated through the parabolic reflector. Subsequently, the light spectrum is divided into two components by the spectrum-splitting optical filter: the solar irradiance that penetrates the filter and reaches PV, $S_{\mathrm{PV}}$, and the solar irradiance that is reflected by the filter and reaches ETA, $S_{\mathrm{ETA}}$:

$$S_{PV} = \rho_{PR}\frac{A_{PR}}{A_{PV}}\int_{280nm}^{4000nm} \tau_F(\lambda)G(\lambda,t)d\lambda \tag{19}$$

$$S_{ETA} = \rho_{PR}\frac{A_{PR}}{A_{ST}}\int_{280nm}^{4000nm} \rho_F(\lambda)G(\lambda,t)d\lambda \tag{20}$$

where $\tau_{\mathrm{F}}$ the transmittance of the filter, $\rho_{\mathrm{F}}$ the reflection of the filter, $A_{\mathrm{PR}}$ the area of the parabolic reflector, $A_{\mathrm{PV}}$ the area of the PV, $A_{\mathrm{ST}}$ the area of the inner solar thermal absorber of the ETA, $\rho_{\mathrm{PR}}$ is the reflection of the parabolic reflector. The ratio of the area of the parabolic reflector and the area of ST inside ETA determines the geometric concentration ratio for ETA. Due to the difference in the surface area between the outer glass and the inner solar thermal absorber of the ETA, the solar irradiance experienced by the outer glass, $S_{\mathrm{ETA,og}}$:

$$S_{\mathrm{ETA,og}} = \rho_{\mathrm{PR}}\frac{A_{\mathrm{PR}}}{A_{\mathrm{og}}}\int_{280\mathrm{nm}}^{4000\mathrm{nm}} \rho_{\mathrm{F}}(\lambda)G(\lambda,t)\mathrm{d}\lambda \tag{21}$$

where $A_{\mathrm{og}}$ is the area of the outer glass of the ETA. Assuming that the spectrum-splitting optical filter splits light ideally and its absorption loss is 5% [34,35]. Then the values of $\tau_{\mathrm{F}}$ and $\rho_{\mathrm{F}}$ are:

$$\tau_{\mathrm{F}}(\lambda) = \begin{cases} 0.95\lambda < \lambda_{\mathrm{cut}} \\ 0\lambda > \lambda_{\mathrm{cut}} \end{cases} \tag{22}$$

$$\rho_{\mathrm{F}}(\lambda) = \begin{cases} 0\lambda < \lambda_{\mathrm{cut}} \\ 0.95\lambda > \lambda_{\mathrm{cut}} \end{cases} \tag{23}$$

where $\lambda_{\mathrm{cut}}$ is the cutting edge of the spectrum-splitting filter ($\lambda_{\mathrm{cut}}$ = 900 nm in this study).

#### 3.2.2. Electrical model: PV

Firstly, the dark saturation current, $J_{\mathrm{ds}}$, is calculated as [29]:

$$J_{\mathrm{ds}} = k_1 T_{\mathrm{std}}^{\frac{3}{z}} \exp\left(\frac{-E_g}{bk_{\mathrm{B}}T_{\mathrm{std}}}\right) \tag{24}$$

where $k_1$, $b$ and $z$ are empirical parameters for PV ($k_1$ = 0.03, $b$ = 1.2, and $z$ = 0.98) [29], $E_g$ is the band gap energy for PV material, $k_{\mathrm{B}}$ the Boltzmann constant ($1.380649\times10^{-23}$ J K$^{-1}$), and $T_{\mathrm{std}}$ is the standard temperature of PV (*i.e.*, 298.15 K). The light generated current, $J_{\mathrm{L}}$, is determined by integrating the spectral response of the PV cells as:

$$J_{\mathrm{L}} = \rho_{\mathrm{PR}}\frac{A_{\mathrm{PR}}}{A_{\mathrm{PV}}}\tau_g\alpha_{\mathrm{PV}}A_{\mathrm{cell}}\int_{280}^{4000} \tau_{\mathrm{F}}(\lambda)G(\lambda,t)SR(\lambda)\mathrm{d}\lambda \tag{25}$$

where $SR(\lambda)$ is the spectral response of PV, $G(\lambda,t)$ is the incident spectrum, $\tau_g$ is the transmittance of the glass covering the PV and $\alpha_{\mathrm{PV}}$ is the absorptance of PV. All the optical losses of the parabolic reflector, spectral-splitting filter, cover glass of PV and solar cell surface are considered, and $A_{\mathrm{cell}}$ is the area of one PV cell in PV module. The short-circuit current, $J_{\mathrm{sc}}$, is given by:

$$J_{\mathrm{SC}} = A_j J_{\mathrm{L}} \tag{26}$$

where $A_{\mathrm{j}}$ is the ideality factor for short-circuit current ($A_{\mathrm{j}}$ = 0.97 in this study) [36]. The relationship between the voltage, $V$, and current of each cell, $J$, can be derived from the ideal diode equation:

$$J = J_{\mathrm{sc}} - J_{\mathrm{ds}}\exp\left[\frac{eV}{A'k_{\mathrm{B}}T_{\mathrm{std}}}\right] \tag{27}$$

where $A'$ is the PV cell ideality factor ($A'$ =1 in this study) [29], $e$ is the charge of an electron. The *I-V* curve of the PV module is derived by interconnecting multiple PV cells in series and/or parallel configurations. Assuming negligible wire losses in this study, the performance parameter translation from a single cell to the entire module is considered to be unity:

$$I_{PV} = JN_{p\_PV} \tag{28}$$

$$V_{PV} = VN_{s\_PV} \tag{29}$$

where $N_{p\_PV}$ and $N_{s\_PV}$ are the numbers of PV cells connected in parallel and series ($N_{p\_PV}$ = 2 and $N_{s\_PV}$ = 30 in this study). The influence of temperature on PV performance primarily manifests in three aspects: current, voltage, and fill factor (*FF*). Notably, the effect of temperature elevation on voltage surpasses its impact on current [36,37]. The open-circuit voltage ($V_{oc}$) at various temperatures can be determined using:

$$V_{oc} = V_{oc\_std}(1 + \beta_V(T_{PV} - T_{std}))$$ (30)

where $V_{oc\_std}$ is the open circuit voltage at standard temperature, and $\beta_v$ is the temperature coefficient of voltage ($\beta_v$ = -0.14 %/°C in this study [38]), $T_{PV}$ is the temperature of PV panel under the working condition, and $T_{std}$ is the standard temperature, in this study, it is 25 °C. The effect of temperature on short circuit current ($I_{sc}$) and *FF* can be calculated in the same way:

$$I_{SC} = I_{sc\_std}(1 + \beta_I(T_{PV} - T_{std}))$$ (31)

$$FF = FF_{std}(1 + \beta_{FF}(T_{PV} - T_{std}))$$ (32)

where $I_{sc\_std}$ and $F_{std}$ are the short circuit current and fill factor at standard temperature, and $\beta_I$ and $\beta_{FF}$ are the temperature coefficients of current and fill factor ($\beta_I$ = 0.07%/°C and $\beta_{FF}$ = -0.01%/°C in this study [38]). The final effect of temperature on efficiency can be seen as the sum of the effects of temperature on the three [11]:

$$\beta_{Eff} = \beta_{FF} + \beta_I + \beta_V$$ (33)

After determining the short-circuit current and open-circuit voltage, another important point to determine is the MPP, which can be calculated via the fill factor:

$$FF = \frac{V_{MPP}I_{MPP}}{V_{oc}I_{SC}}$$ (34)

Since the effect of temperature on voltage is much greater than its effect on current [36,37], the current at MPP can be expressed by Anderson translation equation [39]:

$$I_{MPP} = I_{MPP\_std}(1 + \beta_I(T_{PV} - T_{std}))$$ (35)

where $I_{MPP\_std}$ is the MPP current at standard temperature. By substituting the above equations for $V_{oc}$, $I_{sc}$, and $I_{MPP}$ into the equation for *FF*, the MPP voltage value at different temperatures, $V_{MPP}$ can be calculated:

$$V_{MPP} = V_{MPP\_std}(1 + \beta_{FF}(T_{PV} - T_{std}))(1 + \beta_V(T_{PV} - T_{std}))$$ (36)

### 3.2.3. Electrical model: electrolyzer

In this model, the electrodes of the electrolyzer are polished flat nickel. The pressure of electrolyzer at each temperature is the minimum value that prevents the boiling of the electrolyte. An electrochemical model of electrolysis can be used to describe the *I-V* relationship of an electrolyzer. The voltage required for the electrolysis reaction consists of the following components [26]:

$$V(j,T) = E_0(T) + V'_{ohmic}(j,T) + V'_{HER}(j,T) + V'_{OER}(j,T) + V'_{con} + V'_{bub}$$ (37)

where $E_0(T)$ is the starting potential (*i.e.*, the minimum potential required for the electrolysis reaction to occur, $V'_{ohmic}(j, T)$ is the ohmic losses overpotential of the electrolyte, which is the overpotential required to overcome the resistance between electrodes filled with liquid electrolyte, $V'_{HER}(j, T)$ and $V'_{OER}(j, T)$ are hydrogen evolution reaction and oxygen evolution reaction overpotentials, $V'_{con}$ is the overpotential due to the dissolved gas concentration, and $V'_{bub}$ is the overpotential due to bubble evolution. The influence of concentration and bubble overpotentials on the electrochemical reaction is small at the high electrolyte flow rates considered in this study [26]. Therefore, $V'_{con}$ and $V'_{bub}$ are not considered in the calculations:

$$V(j,T) = E_0(T) + V'_{ohmic}(j,T) + V'_{HER}(j,T) + V'_{OER}(j,T)$$ (38)

the starting potential is a function of the Gibbs free energy change according to Faraday's constant and the reversible cell potential relation:

$$E_0(T) = \frac{\Delta G(T)}{nF}$$ (39)

where $\Delta G(T)$ is the change in Gibbs free energy in the water splitting reaction (*e.g.*, +237.2 kJ/mol $H_2O$ or $H_2$ at 25 °C); $n$ is the number of exchanged electrons in the reaction ($n$ = 2 for each molecule of $H_2$ produced in water splitting reaction) [16]; $F$ is Faraday's constant (*i.e.*, the total charge carried by one mole of electrons, 96485 C/mol $e^-$). The value of $E_0$ is 1.23 V under standard conditions (298.15 K, 1 atm) [26]. The values of $E_0(T)$ at different temperatures are based on data from previous studies [40]. Ohmic losses are calculated as follows:

$$V'_{ohmic}(j,T) = \frac{jW}{\sigma'(T)}$$ (40)

where $j$ is the current density, $W$ is the interelectrode distance (2.5 mm in this study), and σ'($T$) is the conductivity of the electrolyte. The electrolyte is KOH in squeous solution at a concentration of 30 % (w/w) in this study, with $\sigma'$ = 610 mS·cm$^{-1}$ at 30 °C. Values of $\sigma'(T)$ at different temperatures refer to previous research [41]. The activation overpotentials of the hydrogen evolution reaction (HER) and the oxygen evolution reaction (OER) are calculated by the Tafel equation respectively [42,43]:

$$V'_{HER}(j,T) = \beta_{HER}(T)\log\left(\frac{j}{j_{0\_HER}(T)}\right)$$ (41)

$$V'_{OER}(j,T) = \beta_{OER}(T)\log\left(\frac{j}{j_{0\_OER}(T)}\right)$$ (42)

where $j_{0\_HER}(T)$ and $j_{0\_OER}(T)$ are the respective exchange current densities, $\beta_{HER}(T)$ and $\beta_{OER}(T)$ are the Tafel slopes for each reaction. For the HER in KOH solution on nickel electrode at different temperatures, $j_{0\_HER}(T)$ and $\beta_{HER}(T)$ could be found in previous research [42,43], (*i.e.*, at 30 °C, $\beta_{HER}$ is 0.12 V/dec and $j_{0\_HER}$ is $1\times10^{-5}$ A/cm$^2$) and the OER on nickel electrodes in KOH solutions at different temperatures is also studied to get the $j_{0\_OER}(T)$ and $\beta_{OER}(T)$ [44].

In the above calculations, the free energy change ($\Delta G(T)$), conductivity of the KOH solution ($\sigma'(T)$), exchange current densities ($j_{0\_HER}(T)$, $j_{0\_OER}(T)$) and Tafel slopes ($\beta_{HER}(T)$, $\beta_{OER}(T)$) are all functions of the temperature. Therefore, the *j-V* curves at different temperatures can then be calculated from the parameters at respective temperatures. The membrane-less gas-separation principle adopted in this model is based on the authors' previous experimental studies [26,27], in which gas crossover was maintained below 1%, leading to high hydrogen purities under controlled electrolyte-flow conditions. The present system-level model does not explicitly resolve gas-separation dynamics, electrolyte and pressure-management hardware, corrosion, or safety-control systems. Long-duration validation under the selected temperature, KOH concentration, pressure, and cycling conditions remains necessary and should be addressed in future experimental work.

After the above calculation, the *j-V* (current density – voltage) curve

can be obtained. For the *I-V* (current – voltage) relationship of each cell, the current can be calculated from:

$$I_{\mathrm{EC\_cell}} = jA_{\mathrm{ele}} \tag{43}$$

where $A_{\mathrm{ele}}$ is the electrode area (5 $cm^2$ for each electrolyzer cell in this study). For each electrolyzer stack, the overall *I-V* curve depends on the number of cells connected in series, $N_{\mathrm{s\_EC}}$ of 18, in each unit, and the number of units connected in parallel, $N_{\mathrm{p\_EC}}$ of 13 in the stack, as described before. The value of $N_{\mathrm{s\_EC}}$ depends on the *I-V* curve of the PV under ideal conditions, so that the OP is as close to the MPP as possible. The value of $N_{\mathrm{p\_EC}}$ depends on the target current density of the electrolyzer. The overall current and voltage calculations are:

$$I_{\mathrm{EC\_stack}} = I_{\mathrm{EC\_cell}} N_{\mathrm{p\_EC}} \tag{44}$$

$$V_{\mathrm{EC\_stack}} = V_{\mathrm{EC\_cell}} N_{\mathrm{s\_EC}} \tag{45}$$

To account explicitly for the power conversion and coupling between the PV module and the electrolyzer stack, a DC–DC converter is incorporated into the electrical model. At each calculation time step, ideal MPP tracking (MPPT) is assumed, so that the PV module operates at its instantaneous MPP under the corresponding irradiance and PV temperature. The DC–DC converter output is subsequently matched to the temperature-dependent *I–V* curve of the electrolyzer stack. Accordingly, the electrical power balance between the PV module and the electrolyzer stack is expressed as:

$$V_{\mathrm{EC\_stack}}(t) I_{\mathrm{EC\_stack}}(t) = \eta_{\mathrm{DC-DC}} V_{\mathrm{MPP}}(t) I_{\mathrm{MPP}}(t) \tag{46}$$

where $\eta_{\mathrm{DC\text{-}DC}}$ is the conversion efficiency of the DC–DC converter, which is assumed to remain constant at 95% in this study; $V_{\mathrm{mpp}}(t)$ and $I_{\mathrm{mpp}}(t)$ are the voltage and current of the PV module at its instantaneous MPP, respectively; and $V_{\mathrm{EC\_stack}}(t)$ and $I_{\mathrm{EC\_stack}}(t)$ are the operating voltage and current of the electrolyzer stack after DC–DC conversion, respectively. The electrolyzer operating point is determined by satisfying Eq. (46) together with its temperature-dependent *I–V* relationship. Therefore, the PV module is maintained at its MPP, while the 5% DC–DC conversion loss is explicitly included in the electrolyzer input power and the calculated hydrogen production. The converter efficiency is assumed to be constant over the active operating range, while manufacturer-specific part-load efficiency variations and sub-hourly MPPT dynamics are not resolved.

### 3.2.4. System thermal model

The thermal model is based on the law of energy balance for each component. Detailed energy-balance equations for the glazing glass surrounding the PV module, the PV module, are introduced below.

The energy input of the glazing glass is the absorbed solar irradiance $Q_{\mathrm{in,g}}$, which comes from incident sunlight and reflection light from the PV module. The energy output includes radiative and convective heat transfer to the ambient, $Q_{\mathrm{r,g-sky}}$ and $Q_{\mathrm{conv,g-a}}$, respectively, and conductive and radiative heat transfer to the PV module, $Q_{\mathrm{cd,g-PV}}$ and $Q_{\mathrm{r,g-PV}}$. The energy balance equation for the glazing glass surrounding the PV module is expressed as:

$$Q_{\mathrm{in,g}} = Q_{\mathrm{r,g-sky}} + Q_{\mathrm{conv,g-a}} + Q_{\mathrm{cd,g-PV}} + Q_{\mathrm{r,g-PV}} \tag{47}$$

corresponding to:

$$\begin{aligned} A_{\mathrm{PV}}\alpha_{\mathrm{g}} S_{\mathrm{PV}}\left(1+\tau_{\mathrm{g}}\rho_{\mathrm{PV}}\right) &= \varepsilon_{\mathrm{g}}\sigma A_{\mathrm{PV}}\left(T_{\mathrm{g}}^4 - T_{\mathrm{sky}}^4\right) \\ +h_{\mathrm{wind}} A_{\mathrm{PV}}\left(T_{\mathrm{g}} - T_{\mathrm{a}}\right) + h_{\mathrm{cd,g-PV}} A_{\mathrm{PV}}\left(T_{\mathrm{g}} - T_{\mathrm{PV}}\right) &+ \frac{A_{\mathrm{PV}}\sigma\left(T_{\mathrm{g}}^4 - T_{\mathrm{PV}}^4\right)}{\frac{1}{\varepsilon_{\mathrm{PV}}} + \frac{1}{\varepsilon_{\mathrm{g}}} - 1} \end{aligned} \tag{48}$$

where $S_{\mathrm{PV}}$ is the solar irradiance, $A_{\mathrm{PV}}$ is the surface area of PV module (the same as the area of the glazing glass), $\alpha_{\mathrm{g}}$ is the absorptance of glazing glass ($\alpha_{\mathrm{g}} = 0.03$ [29]), $\tau_{\mathrm{g}}$ is the transmittance of the glazing glass ($\tau_{\mathrm{g}} = 0.95$ [29]), $\rho_{\mathrm{PV}}$ is the reflectance of PV module ($\rho_{\mathrm{PV}} = 0.07$ [29]), $\sigma$ is the Stefan–Boltzmann constant ($5.67\times10^{-8}$ W $m^{-2}K^{-4}$), $\varepsilon_{\mathrm{g}}$ is the emissivity of glass ($\varepsilon_{\mathrm{g}} = 0.9$ [29]), and $\varepsilon_{\mathrm{pv}}$ is the emissivity of the PV module ($\varepsilon_{\mathrm{pv}} = 0.9$ [45]). The variables $T_{\mathrm{g}}$, $T_{\mathrm{PV}}$, $T_{\mathrm{a}}$ and $T_{\mathrm{sky}}$ are cover glass, PV, ambient and sky temperatures respectively. The sky temperature $T_{\mathrm{sky}}$ is expressed as $T_{\mathrm{sky}} = 0.0552T_{\mathrm{a}}^{1.5}$[46]. The heat convection coefficient to the ambient, $h_{\mathrm{wind}}$, is a function of wind speed [47]. The heat transfer coefficient between the glazing glass and the PV module, $h_{\mathrm{cd,g\text{-}PV}}$, is dominated by the heat conduction of the air gap between the glazing glass ang the PV module [47]. The energy balance for the PV module is:

$$Q_{\mathrm{in,\ PV}} + Q_{\mathrm{cd,g-PV}} + Q_{\mathrm{r,g-PV}} = Q_{\mathrm{ele-PV}} + Q_{\mathrm{conv,PV-HTF}} \tag{49}$$

corresponding to:

$$\begin{aligned} &A_{\mathrm{PV}}\alpha_{\mathrm{pv}}\tau_{\mathrm{g}} S_{\mathrm{PV}} + h_{\mathrm{cd,g-PV}} A_{\mathrm{PV}}\left(T_{\mathrm{g}} - T_{\mathrm{PV}}\right) + \frac{A_{\mathrm{PV}}\sigma\left(T_{\mathrm{g}}^4 - T_{\mathrm{PV}}^4\right)}{\frac{1}{\varepsilon_{\mathrm{PV}}} + \frac{1}{\varepsilon_{\mathrm{g}}} - 1} \\ &\quad = \eta_{\mathrm{ele}}\tau_{\mathrm{g}} G_{\mathrm{PV}} A_{\mathrm{PV}} + h_{\mathrm{conv,PV-HTF}} A_{\mathrm{pv}}\left(T_{\mathrm{PV}} - T_{\mathrm{ave,HTF}}\right) \end{aligned} \tag{50}$$

where $\eta_{\mathrm{ele}}$ is the electrical efficiency of PV module, and $h_{\mathrm{conv,PV\text{-}HTF}}$ is the convective heat transfer coefficient between the PV module and the HTF in the cooling channel [29]. The average temperature of the HTF in the cooling channel is:

$$T_{\mathrm{ave,\ HTF}} = \frac{T_{\mathrm{out,PV}} + T_{\mathrm{in,PV}}}{2} \tag{51}$$

where $T_{\mathrm{out,PV}}$ and $T_{\mathrm{in,PV}}$ are the outlet and inlet temperature of HTF in the cooling channel. The energy balance for the HTF in the cooling channel is:

$$Q_{\mathrm{conv,PV-HTF}} = Q_{\mathrm{gain,\ HTF}} + Q_{\mathrm{loss,PV-a}} \tag{52}$$

corresponding to:

$$\begin{aligned} h_{\mathrm{conv,PV-HTF}} A_{\mathrm{PV}}\left(T_{\mathrm{PV}} - T_{\mathrm{ave,HTF}}\right) &= \dot{m}_{\mathrm{HTF}} c_{\mathrm{HTF}}\left(T_{\mathrm{out,PV}} - T_{\mathrm{in,PV}}\right) \\ &+ h_{\mathrm{loss,HTF-a}} A_{\mathrm{PV}}\left(T_{\mathrm{ave,\ HTF}} - T_{\mathrm{a}}\right) \end{aligned} \tag{53}$$

where $h_{\mathrm{conv,PV\text{-}HTF}}$ is the heat transfer coefficient between the PV module and the HTF in the cooling channel, $\dot{m}_{\mathrm{HTF}}$ is the mass flow rate, $c_{\mathrm{HTF}}$ is the specific heat capacity of the HTF (water as HTF for PV cooling, 4186 J/(kg·K) at around 50 °C [48]), $h_{\mathrm{loss,HTF\text{-}a}}$ is the equivalent heat transfer coefficient between the HTF and the ambient. Additionally, all heat losses incurred during fluid flow through the connection piping are accounted for by employing the subsequent energy balance equation to determine the temperature of the outflow:

$$\dot{m}_i c_i\left(T_{\mathrm{out,i}} - T_{\mathrm{in,i}}\right) = h_{\mathrm{loss,pipe-a}} A_{\mathrm{p}}\left(\frac{T_{\mathrm{out,i}} + T_{\mathrm{in,i}}}{2} - T_{\mathrm{a}}\right) \tag{54}$$

where $\dot{m}_i$ and $c_i$ are the mass flow rate and specific heat capacity of the fluid in a pipe, for cooling water, $c_{\mathrm{water}}$ is 4186 J/(kg·K), for HTF in the ETA at around 180 °C, $c_{\mathrm{HTF}}$ is 2663 J/(kg·K) [49], $T_{\mathrm{out,i}}$ and $T_{\mathrm{in,i}}$ are the outlet and inlet of a connection pipe, $A_{\mathrm{p}}$ is the surface area of a pipe (set as 1 $m^2$ in this study), and $h_{\mathrm{loss,pipe\text{-}a}}$ is the equivalent heat transfer coefficient between the HTF and the ambient.

Given the absence of thermal coupling between PV and the ETA, the thermal management strategy for the PV system is designed exclusively for active cooling to maximize photovoltaic conversion efficiency, rather than for thermal energy recovery. Consequently, the coolant flow rate is increased to minimize the temperature rise across the module, maintaining the outlet fluid temperature at a limit of 21 °C. In this configuration, HX1 serves solely as a heat dissipation unit to reject low-grade waste heat to the environment, modelled using the common logarithmic average temperature difference (LMTD) method [50]. The energy balance of outer glass of the ETA includes absorbed solar irradiance, $Q_{\mathrm{og}}$,

the radiative heat from the inner solar thermal absorber, $Q_{r,og\text{-}ST}$, radiative heat loss, $Q_{r,og\text{-}sky}$, and convective heat loss, $Q_{conv,og\text{-}sky}$ to the environment:

$$Q_{og} = Q_{r,og-sky} + Q_{conv,og-a} + Q_{r,og-ST} \tag{55}$$

corresponding to:

$$A_{og}\alpha_g S_{ETA,og}\left(1+\tau_g\rho_{ST}\right) = \varepsilon_g\sigma A_{og}\left(T_g^4 - T_a^4\right) + h_{wind}A_{og}\left(T_g - T_a\right) + \frac{A_{og}\sigma\left(T_g^4 - T_{ST}^4\right)}{\frac{1}{\varepsilon_{ST}}+\frac{1}{\varepsilon_g}-1} \tag{56}$$

where $\rho_{ST}$ (0.08) and $\varepsilon_{ST}$ (0.08) are the reflectance and emissivity of the solar thermal absorber [29], $T_{ST}$ is the average temperature of solar thermal absorber. The energy balance of solar thermal absorber consists of absorbed solar irradiance, $Q_{ST}$, radiative heat to outer glass, $Q_{r,og\text{-}ST}$, and conductively heat to the HTF, $Q_{conv,ST\text{-}HTF}$ is:

$$Q_{ST} + Q_{r,og-ST} = Q_{conv,ST-HTF} \tag{57}$$

corresponding to:

$$A_{ST}\alpha_{ST}\tau_g S_{ETA} + \frac{A_{ST}\sigma\left(T_g^4 - T_{ST}^4\right)}{\frac{1}{\varepsilon_{ST}}+\frac{1}{\varepsilon_g}-1} = h_{conv,ST-HTF}A_{ST}\left(T_{ST} - T_{ave,ETA}\right) \tag{58}$$

where $T_{ave,EAT}$ is the average temperature of inlet, $T_{in,ETA}$, and outlet temperature, $T_{out,ETA}$, of HTF through ST channel:

$$T_{ave,ETA} = \frac{T_{out,ETA} + T_{in,ETA}}{2} \tag{59}$$

The $h_{conv,ST\text{-}HTF}$ is the heat transfer coefficient for $Q_{conv,ST\text{-}HTF}$. The convective heat transfer coefficient can be estimated based on the Nusselt number:

$$h_{conv,ST-HTF} = \frac{Nu \times k_{HTF}}{D_{ST}} \tag{60}$$

where the $Nu$ is 3.66 the cylindrical pipes used in ETA with laminar flow [29,47], $D_{ST}$ is the diameter of the inner tube of the ETA (2.8 cm), and $k_{HTF}$ is thermal conductivity of the HTF (0.12 W·(m/K) [49]). Upon establishing the energy balance of the ETA, the heated HTF is conveyed via pipes to the HX2, where it is utilized to heat the electrolyte. The LMTD method is used to model the heat exchange process of HX2 [50]. Thermal energy input inside the electrolyzer is only generated through the overpotential during electrolysis, $Q_{heat,EC}$. which is used to heat the electrolyte (KOH solution), $Q_{conv,EC\text{-}KOH}$ as well as heat loss to the environment, $Q_{conv,EC\text{-}a}$. The energy balance in the electrolyzer is expressed as:

$$Q_{heat,EC} = Q_{conv,EC-KOH} + Q_{conv,EC-a} \tag{61}$$

corresponding to:

$$I_{wp}\left(V_{wp} - V_{TN}N_{S\_EC}\right) = \dot{m}_{EC}c_{EC}\left(T_{out,EC} - T_{in,EC}\right) + A_{EC}h_{loss,EC-a}\left(T_{ave,EC} - T_a\right) \tag{62}$$

$$T_{ave,EC} = \frac{T_{in,EC} + T_{out,EC}}{2} \tag{63}$$

where $I_{wp}$ is the working current of electrolyzer stack, $V_{wp}$ is the working voltage of electrolyzer stack, $V_{TN}$ is the thermal neutral voltage of electrolytic water reaction (*i.e.*, minimal variation with temperature and is considered as a constant in this study, set at 1.48 V [51]), $\dot{m}_{EC}$ is the flow rate of the electrolyte, $c_{EC}$ is the specific heat capacity of electrolyte (3.28 kJ/kg/K), $T_{in,EC}$ is the temperature of the electrolyte at the electrolyzer inlet, $T_{out,EC}$ is the temperature of the electrolyte at the electrolyzer outlet. The temperature of the entire electrolyzer stack is considered as uniformly distributed, and its temperature, $T_{ave\_EC}$, is the average temperature of the electrolyte inside the electrolyzer, and $A_{EC}$ is the surface area of the entire electrolyzer stack. The $h_{loss,\ EC-a}$ is the equivalent heat transfer coefficient for $Q_{conv,EC-a}$ is:

$$h_{loss,ec-a} = \frac{1}{\frac{W_{shell}}{k_{shell}} + \frac{W_{insu,EC}}{k_{insu,EC}} + \frac{1}{h_{wind}}} \tag{64}$$

where $W_{shell}$ (2 mm) and $W_{insu,EC}$ (2 cm) are the thickness of shell layer and insulation layer of electrolyzer, and $k_{shell}$ (30 W·(m/K) [52]) and $k_{insu,EC}$ (0.035 W·(m/K) [53]) are the thermal conductivity of them.

Additional water needs to be added into the electrolyte to make up for the water consumed in the hydrogen production process. After adding additional water, the temperature is calculated as:

$$T_{out,EC\_mix} = \frac{\dot{m}_{loss}}{\dot{m}_{EC}}T_{in,EC\_mix} + \frac{\dot{m}_{EC} - \dot{m}_{loss}}{\dot{m}_{EC}}T_{out,EC} \tag{65}$$

where $T_{out,EC\_mix}$ is the electrolyte temperature after mixing additional water, $T_{in,EC\_mix}$ is the temperature of additional cold water, set as 20 °C in this study, and $\dot{m}_{EC}$ is the flow rate of consumed water in the electrolyzer (the same as the additional water). The thermal-loss parameters, including the pipe surface area, insulation characteristics, convective heat-transfer correlations, and heat-exchanger effectiveness, were adopted from the previously developed SSPVTH system design [45] and applied consistently across all locations and tracking configurations. These simplified assumptions may affect the absolute operating temperatures and hydrogen yields under site-specific piping layouts and wind conditions, but their consistent application enables an unbiased relative comparison between locations and tracking strategies. Future work should incorporate site-specific thermal-loss parameters and evaluate their influence through dedicated sensitivity analyses and experimental calibration.

### 3.3. Solar hydrogen production model

The evaluation of solar hydrogen production adopts a hierarchical time-resolved simulation framework. This process progresses from instantaneous system performance to monthly aggregation, and finally to the annualized hydrogen yield.

The primary meteorological input is the effective broadband irradiance, $S_{real}(t)$, as defined in Section 3.2. This variable accounts for the specific tracking strategy, corresponding to $DNI_{DA}(t)$ for the dual axis baseline and the projected $DNI_{SA}(t)$ for the single axis configuration. To characterize the seasonal performance variations, monthly average diurnal profiles are utilized. For each calendar month, the hourly irradiance and ambient temperature profiles are constructed by averaging the historical data over all days in that month, thereby capturing the typical meteorological conditions including stochastic weather variations.

At each time step $t$, the instantaneous hydrogen production rate $\dot{m}_{H2}(t)$ is computed by solving the coupled optical, thermal, and electrochemical sub-models described in previous sections. A minimum irradiance threshold of 45 W/m$^2$ is applied, below which the system is considered inactive. For each active time step, the electrolyzer-stack current is converted into the instantaneous hydrogen mass production rate according to Faraday's law:

$$\dot{m}_{H_2}(t) = \frac{3600N_{s\_EC}\eta_F I_{EC\_stack}M_{H_2}}{nF} \tag{66}$$

where $M_{H2}$ is the molar mass of hydrogen (2.016 g mol$^{-1}$), while the remaining parameters retain the definitions given above, $N_{S\_EC}$ is the number of electrolyzer cells connected in series, $\eta_F$ is the Faradaic efficiency, which is 1 here; $I_{EC\_stack}$ is the operating current of the electrolyzer stack. The factor of 3600 converts the hydrogen production rate from g s$^{-1}$ to g h$^{-1}$. The daily hydrogen mass production calculated from the monthly average daily profile for month *mo,* denoted as $m^{(mo)}_{H_2,day}$, is obtained by integrating the instantaneous production rate over the operating hours:

$$m^{(mo)}_{H_{2,day}} = \sum_t \dot{m}_{H_2}(t) \tag{67}$$

To facilitate a size-independent comparison across different geographic locations and tracking configurations, the production metrics are normalized by the reference optical aperture area ($A_{PR}$). The normalized daily hydrogen yield is defined as:

$$Y^{(mo)}_{H_{2,day}} = \frac{m^{(mo)}_{H_{2,day}}}{A_{PR}} \tag{68}$$

the annual specific hydrogen yield is derived by aggregating the monthly daily yields, weighted by the number of days in each respective month, $N_{mo}$:

$$Y_{H_{2,year}} = \frac{1}{A_{PR}} \sum_{mo=1}^{12} (m^{(mo)}_{H_{2,day}} N_{mo}) \tag{69}$$

this metric serves as the quantitative basis for the subsequent techno-economic analysis, representing the total hydrogen energy produced per unit of collector area over a full meteorological year.

To evaluate the overall energy conversion performance of the system, the annual STH efficiency is adopted as the primary metric. This indicator reflects the long-term yield relative to the available solar resource and is defined as [15,54]:

$$\eta_{STH,\ annual} = \frac{Y_{H2,year} HHV_{H2}}{E_{solar}} \tag{70}$$

where $Y_{H2,year}$ is the annual hydrogen yield (kg/m$^2$/year), $HHV_{H2}$ is the higher heating value [15] of hydrogen (= 39.4 kWh/kg), and $E_{solar}$ is defined as the annual direct normal irradiation (kWh/m$^2$/year) of a site. The STH efficiency is reported on an HHV basis because this accounts for the total energy content of hydrogen, including the latent heat recovered when the product water is condensed. For comparison, using the hydrogen LHV of 33.3 kWh kg$^{-1}$ gives $\eta_{STH,\ LHV} = (33.3/39.4)\ \eta_{STH,\ HHV} \approx 0.845\ \eta_{STH,\ HHV}$.

### 3.4. Techno-economic assessment framework

#### 3.4.1. Overview and assessment scope

The techno-economic performance of the SSPVTH system is evaluated using a discounted cash-flow (DCF) framework, implemented consistently across all investigated sites and tracking configurations. The assessment adopts a system-level perspective, covering a project lifetime of 25 years. The annual hydrogen production is projected based on the techno simulation results above, serving as the baseline for the lifecycle revenue generation. The cost structure is categorized into three primary components: CAPEX, annual operating and maintenance expenditure (OPEX), and scheduled component replacement costs (REPL). The primary economic indicators derived from the model include the LCOH, the component-wise cost breakdown, and the PBT. To evaluate the investment risk and model stability, the robustness of the economic conclusions is examined via one-way sensitivity analysis and Monte Carlo uncertainty analysis for each site–tracker combination. Land costs are not included in this analysis due to their strong location-specific variability and the relatively small system scale considered. Their exclusion primarily affects absolute LCOH values but does not alter the relative comparison between system configurations.

The baseline economic assumptions and specific component costs are detailed in Table 1. The cost inventory is derived from recent market data and relevant literature benchmarks.

#### 3.4.2. Levelized cost of hydrogen

A nominal discounting approach is adopted to ensure consistency between cost escalation and discounting. The LCOH (in €/kg) is then defined as [62]:

$$\mathrm{LCOH} = \frac{PRV_{cost}}{PRV_{H_2}} \tag{71}$$

where $PRV_{H2}$ is present value (PRV) of hydrogen output over the project lifetime, and $PRV_{cost}$ is the total present value of system cost, which is given by:

$$PRV_{cost} = I_0 + PRV_{OPEX} + PRV_{REPL} \tag{72}$$

where $I_0$ is the initial investment CAPEX, $PRV_{OPEX}$ is the present value of lifetime operating expenditure, and $PRV_{REPL}$ is the present value of replacement costs. The present value of replacement costs $PRV_{REPL}$ is calculated as:

$$PRV_{REPL} = \sum_k \frac{C_{k,0}(1+i)^{t_k-1}}{(1+r_{nom})^{t_k}} \tag{73}$$

where $r_{nom}$ is the nominal discount rate, $C_{k,0}$ is the base-year cost, $k$ is the identical number of a replacement event, $t_k$ is the replacement year, and $i$ is the annual inflation rate. Component replacement costs are modelled as discrete expenditures occurring at specific intervals. In this study, a scheduled system overhaul is assumed to occur every 10 years of operation [16]. Each replacement event $k$ is defined by its base-year cost $C_{k,0}$ and also the replacement year $t_k$. The overhaul strategy involves a partial replacement (50%) of the electrolyzer stack and spectral-splitting filters to account for performance degradation, along with a general system refurbishment cost estimated at 5% of the total direct capital cost to cover balance-of-plant maintenance. The nominal discount rate $r_{nom}$ is defined with the Fisher equation [61]:

$$r_{nom} = (1 + r_{real})(1 + i) - 1 \tag{74}$$

where $r_{real}$ is the real discount rate, and $i$ is the annual inflation rate. The present value of the lifetime operating expenditure $PRV_{OPEX}$ is obtained by inflating $OPEX_0$ and discounting it over the lifetime $N$:

**Table 1**
Main economic parameters and capital expenditure assumptions used in the baseline model.

| Component | Unit | Unit Cost, /€ | Quantity | Ref |
|---|---|---|---|---|
| Concentrated PV modules | Area(m$^2$) | 1200 | 0.24 | [55] |
| Parabolic reflector | Area (m$^2$) | 100 | 5.04 | [29] |
| Spectral-splitting filter | Area (m$^2$) | 800 | 0.32 | [29] |
| Evacuated tube absorber | Area (m$^2$) | 100 | 0.24 | [29] |
| Electrolyzer stack | Power (kW) | 350 | 1.0 | [56,57] |
| DC–DC converter | Power (kW) | 50 | 1.0 | [58] |
| Heat exchangers | per unit | 200 | 2 | [29] |
| Pumps | per unit | 100 | 3 | [29] |
| Piping & valves | Lump sum | 100 | 1 | [59] |
| Sensors & controls | Lump sum | 100 | 1 | [59] |
| Thermal oil / HTF | Mass (kg) | 4 | 5.0 | [29] |
| Thermal insulation | Lump sum | 100 | 1 | [29] |
| Electrical balance of system (BOS) | Lump sum | 100 | 1 | [59,60] |
| Single axis tracker | Area (m$^2$) | 40 | 5.04 | [60] |
| Dual axis tracker | Area (m$^2$) | 100 | 5.04 | [60] |

$$PRV_{OPEX} = \sum_{t=1}^{N} \frac{OPEX_0(1+i)^{t-1}}{(1+r_{nom})^t} \quad (75)$$

where $t$ represents the year index. The design lifetime for the whole system is 25 years. The annual operating expenditure is represented by a single equivalent operating cost term, $OPEX_0$. This term is modelled as a fixed percentage of the total CAPEX to capture all recurring costs associated with normal system operation, including auxiliary electricity consumption, insurance, and routine maintenance. Specifically, $OPEX_0$ is set to 1.5% of $I_0$ for the single axis tracking system. For the dual axis configuration, this rate is increased to 2.0% to account for the higher complexity and maintenance requirements of the dual axis tracking mechanism.

The total CAPEX $I_0$ is calculated as:

$$I_0 = C_{\text{direct}} + C_{\text{add}} \quad (76)$$

where $C_{\text{direct}}$ is the total direct component costs, and $C_{\text{add}}$ is a cost adder. The CAPEX $I_0$ is incurred at the beginning of the project ($t = 0$) and comprises the total direct component costs $C_{\text{direct}}$, including PV modules, optical concentrators, spectral filters, absorbers, electrolyzers, power electronics, and tracking structures. To account for balance-of-system expenses, a cost adder $C_{\text{add}}$ covering installation, commissioning, and contingency is applied as a fixed fraction of the direct costs. In this study, $C_{\text{add}}$ is set to 10% of $C_{\text{direct}}$. The direct CAPEX includes the principal solar-collection and conversion components, thermal-loop equipment, electrolyzer stack, power electronics, sensors and controls, electrical balance-of-system equipment, and tracking hardware listed in Table 1. The additional 10% cost adder represents installation, system integration, commissioning, basic optical alignment, and contingency. Site-specific foundations and civil works, land acquisition, comprehensive safety infrastructure, water treatment, and downstream hydrogen drying, purification, compression, storage, transport, and dispensing are excluded. Accordingly, the reported LCOH represents the production cost at the electrolyzer outlet rather than the delivered cost of compressed or stored hydrogen; these exclusions may affect the absolute LCOH but are applied consistently across all sites and tracking configurations.

The present value of hydrogen output over the project lifetime $N$ is calculated by discounting the annual hydrogen production:

$$PRV_{H_2} = \sum_{t=1}^{N} \frac{Y_{H_{2,year}} A_{PR} D_t}{(1+r_{nom})^t} \quad (77)$$

For each investigated site, the annual hydrogen production $Y_{\text{H2,year}}$ is obtained from the system-performance model outputs and used as the basis for the economic calculations. For the degradation sensitivity analysis, this value is treated as the first-year annual hydrogen production, and the hydrogen production in year $t$ is calculated as $Y_{\text{H2},t} = Y_{\text{H2,year}} D_t$, where $D_t = (1\text{-}d)^{at}$ is the annual performance-degradation multiplier, $d$ is the assumed annual system-level degradation rate, and $a_t$ is the effective system age in year $t$, defined as the number of years elapsed since the beginning of the project or since the most recent scheduled replacement. The effective system age starts from zero in the first year, increases annually, and is reset to zero after each 10-year replacement event. Therefore, replacement at the end of years 10 and 20 restores the system output at the beginning of years 11 and 21, respectively. In the base-case calculations $d$=0 and therefore $D_t$ =1 throughout the 25-year project lifetime.

### 3.4.3. Discounted payback time

The economic feasibility is further assessed using the PBT, defined as the time required for the cumulative discounted cash flows to recover the initial capital investment. The PBT is determined as the minimum number of years $\tau$ for which the net present value becomes non-negative:

$$PBT = min\left\{\tau \in \{1,\cdots,N\} \middle| \sum_{t=1}^{\tau} \frac{R_t - (OPEX_t + C_{rep,t})}{(1+r_{nom})^t} \geq I_0\right\} \quad (78)$$

where $I_0$ is the initial investment. The terms $OPEX_t$ and $C_{\text{rep},t}$ represent the nominal cash outflows in year $t$, derived by escalating the base-year operating and replacement costs defined in Section 3.5.1 with the annual inflation rate $i$. Specifically, $C_{\text{rep},t}$ aggregates the inflation-adjusted costs of all components scheduled for replacement in that specific year. The term $R_t$ denotes the nominal annual revenue, which escalates with inflation. To evaluate the economic impact of byproduct valorization, the PBT is calculated under two distinct revenue scenarios:

i) hydrogen sales only, revenue is generated solely from hydrogen production at a retail price of $P_{\text{H2,0}} = 12$ €/kg [63]; this value reflects current market retail rates, but is adopted here assuming a decentralized, on-site generation and utilization scenario, which eliminates the significant distribution and logistics costs associated with centralized production pathways;
ii) hydrogen and oxygen sales, revenue includes the sale of byproduct oxygen at an industrial price of $P_{\text{O2,0}} = 0.15$€/kg [64], assuming a stoichiometric mass ratio of 8:1 for $O_2$:$H_2$.

The annual revenue $R_t$ for the combined scenario is expressed as:

$$R_t = [M_{H_2,t} \cdot P_{H_2,0} + M_{O_2,t} \cdot P_{O_2,0}] \cdot (1+i)^{t-1} \quad (79)$$

where $M_{H_2,t}$ and $M_{O_2,t}$ are the respective production masses in year $t$, accounting for annual system degradation. For the hydrogen-only scenario, the oxygen term in Eq. (79) is set to zero.

To evaluate the robustness of the PBT results to product-price assumptions, an additional deterministic one-way sensitivity analysis was performed for the hydrogen and oxygen selling prices. The baseline prices of hydrogen and oxygen were 12.0 and 0.15 €/kg, respectively. Each price was varied independently by ±20%, while the other price and all technical and economic parameters were held constant. The PBT was recalculated for all four sites and both tracking configurations. The resulting sensitivity was quantified using the difference between the PBT values obtained at −20% and +20% of the corresponding baseline price.

### 3.4.4. Sensitivity and uncertainty analysis

Given the nascent stage of SSPVTH technologies and the volatility of global markets, the economic assessment is subject to inherent uncertainties. To quantify the robustness of the LCOH results and identify dominant cost drivers, a two-tiered stochastic analysis framework was implemented, comprising a deterministic one-at-a-time (OAT) sensitivity analysis and a probabilistic Monte Carlo simulation.

To disentangle the individual impact of specific technical and economic parameters, an OAT sensitivity analysis was performed. In this procedure, key input parameters $x_j$ are perturbed individually by a uniform margin of ± 10% around their baseline values, $x_{j,0}$, while holding all other variables constant:

$$\Delta LCOH_j = |LCOH(1.1 \bullet x_{j,0}) - LCOH(0.9 \bullet x_{j,0})| \quad (80)$$

the resulting sensitivities are ranked and visualized using tornado diagrams, facilitating the identification of the most critical parameters that require rigorous cost control or financing optimization.

While OAT sensitivity analysis highlights individual sensitivities, it fails to capture the non-linear interactions arising from simultaneous parameter variations. To address this, a global Monte Carlo uncertainty analysis was conducted. As detailed in Table 2, six critical stochastic variables were identified, categorized into technological hardware costs and macroeconomic indicators. Since the precise probability density functions (PDFs) for future component costs and market rates are unknown, uniform distributions were assigned to all stochastic variables. This approach adheres to the principle of maximum entropy, avoiding

**Table 2**
Key input parameters and uncertainty ranges for the Monte Carlo simulations.

| Component | Base Value | Uncertainty Range | Perturbation Method |
|---|---|---|---|
| PV modules | 1,200 €/m$^2$ | ± 20 % | Relative Scaling |
| Tracker (Single/ Dual) | 40 /100 €/m$^2$ | ± 20 % | Relative Scaling |
| Spectral-splitting filter | 800 €/m$^2$ | ± 30 % | Relative Scaling |
| Electrolyzer stack | 350 €/kW | ± 30 % | Relative Scaling |
| Real discount rate | 4.0 % | 3 %-7 % | Absolute Range |
| Inflation rate | 2.0 % | 1 %-3 % | Absolute Range |

the introduction of artificial central tendencies or bias that would arise from assuming normal distributions without sufficient empirical data.

The definition of uncertainty ranges relied on a maturity-based classification strategy. For technological parameters, a distinct margin was applied based on commercial readiness. For established technologies with mature supply chains, PV modules and tracking systems, a standard variation of ± 20% was utilized [59]. In contrast, for novel or specialized components, namely the spectral-splitting filters and the membraneless electrolyzer stack, a wider uncertainty margin of ± 30% was assigned to account for the higher unpredictability in their future manufacturing costs and market scaling [65]. For the macroeconomic parameters, the ranges for the real discount rate and inflation were empirically derived from historical financial market volatility [29,66], defining absolute intervals that encompass both conservative and optimistic financing scenarios.

The calculation was executed with $N = 5000$ iterations for each site and tracking configuration to ensure statistical convergence. In each iteration $k$, a random set of input parameters vector $x_k$ is sampled from the prescribed distributions, and the full discounted cash flow model is evaluated to compute the corresponding $LCOH_k$. The resulting dataset of 5000 LCOH outcomes is then aggregated to construct PDFs and calculate risk metrics, such as the P50 (median) value and standard deviation, thereby quantifying the investment risk profile of the SSPVTH system.

## 4. Results and discussion

### 4.1. System performance and annual hydrogen production

To quantify the dynamic response of the SSPVTH system under varying climatic conditions and tracking strategies, hourly hydrogen production rates were calculated using the monthly average daily profile for each month. The diurnal profiles for January and July as illustrative examples of seasonal extremes are shown in Fig. 6. The results reveal distinct seasonal dynamics driven by latitude and local DNI resources. A general trend of narrowed operational time windows and reduced peak production rates during winter is observed across Karlsruhe, Barcelona, and Cairo, directly corresponding to the seasonal decline in solar availability in these regions. However, the severity of this decline differs markedly. Karlsruhe in Fig. 6**(a)** experiences a severe seasonal collapse, where the winter peak falls below 1.2 g/m$^2$/h. In contrast, Barcelona in Fig. 6**(b)** demonstrates significantly better winter resilience; thanks to its relatively high winter DNI compared to Central Europe, its January peak production reduction is far less drastic than that of Karlsruhe.

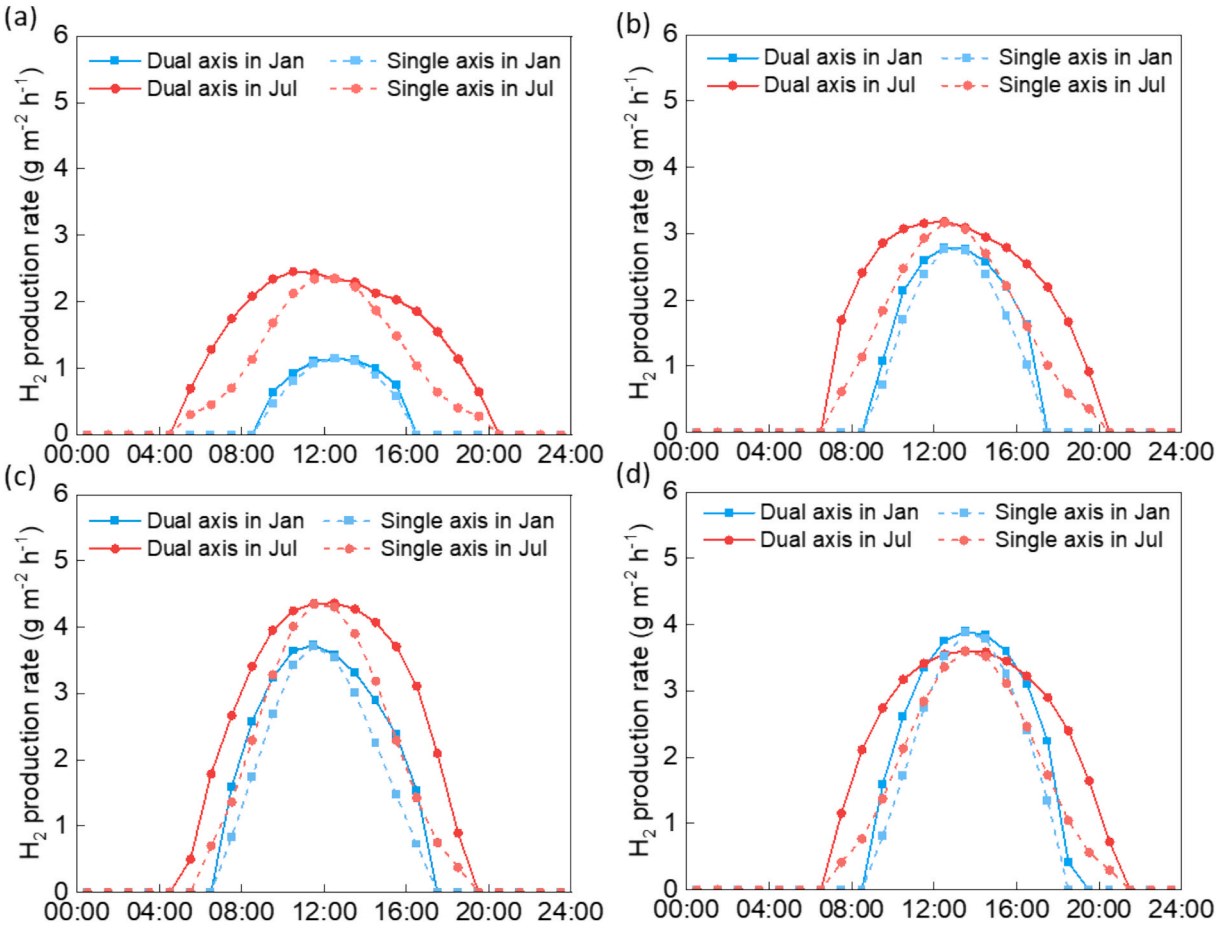


**Fig. 6. Hourly hydrogen production rates in January and July across the four study sites: (a) Karlsruhe, (b) Barcelona, (c) Cairo, and (d) Dunhuang.** Solid lines indicate the performance of the dual axis tracking system, while dashed lines represent the single axis tracking system. The gap between the solid and dashed lines illustrates the production loss due to optical incidence angle misalignment in the single axis configuration.

Moving further south, Cairo in Fig. 6**(c)** achieves the highest summer output of 4.4 g/m$^2$/h while retaining a substantial performance of 3.7 g/m$^2$/h in January. Deviating from this pattern, Dunhuang in Fig. 6**(d)** exhibits a unique inversion phenomenon where the peak production rate at noon in January actually surpasses that in July. A comparison of the July and January profiles in Fig. 3 and Fig. 4, respectively, shows that although the January irradiance profile is narrower because of the shorter daylight duration, its near-noon DNI reaches 786.7 W m$^{-2}$, compared with 708.3 W m$^{-2}$ in July, representing an increase of 11.1%. At the corresponding peak hour, the ambient temperature is −3.9 °C in January and 31.6 °C in July. The higher January DNI changes the electrical operating point of the PV system, while the substantially lower ambient temperature limits the increase in PV operating temperature. Under the combined effects of irradiance and temperature, the calculated PV operating temperature is 45.7 °C in January, compared with 47.8 °C in July, and the PV conversion efficiency increases modestly from 23.9% in July to 24.2% in January. Consequently, the peak normalized hydrogen production rate increases from 3.6 to 3.9 g $H_2$ m$^{-2}$ h$^{-1}$, corresponding to an increase of 8.0%. These quantitative results confirm that the inversion is primarily caused by the higher January DNI, together with the combined influence of irradiance and ambient temperature on PV conversion efficiency. Furthermore, the divergence between the dual axis and single axis curves visually quantifies the yield loss caused by optical misalignment. It is important to note that this simulation explicitly accounts for the time-dependent incidence angles, calculating the dynamic cosine losses at each time step rather than applying a static reduction factor. The dual axis configuration effectively broadens the high-production window by mitigating incidence angle losses during the early morning and late afternoon shoulder hours, a gain particularly pronounced in summer. Conversely, during winter in high-latitude regions like Karlsruhe, the marginal benefit of dual axis tracking diminishes. Due to the restricted solar azimuth sweep and low solar elevation, the geometric advantage of dual axis tracking is constrained, resulting in minimal yield differentiation compared to the single axis baseline during these low-irradiance periods.

Aggregating these hourly rates into a monthly timeframe highlights the critical implications for industrial supply security. The monthly hydrogen yield profiles are shown in Fig. 7, revealing a fundamental divergence in seasonal consistency. A distinct seasonal pattern is observed across Karlsruhe, Barcelona, and Cairo, characterized by a visible production decline during the winter months, albeit with varying degrees of severity. Karlsruhe in Fig. 7**(a)** displays a steep bell-shaped profile with extreme disparity, in July the dual axis average H2 production is 840 g/m$^2$/month, while in January it is 207 g/m$^2$/month, where summer yields are nearly four times higher than winter yields. Moving to lower latitudes, Barcelona in Fig. 7**(b)** and Cairo in Fig. 7**(c)** benefit from higher absolute irradiation, resulting in significantly larger total yields. For Barcelona, the dual axis average H2 production in July is 1008 g/m$^2$/month, while in January it is 550 g/m$^2$/month. However, they nevertheless adhere to the typical solar seasonality, with Cairo's winter output still showing a noticeable reduction compared to its summer peak of approximately 1346 g/m$^2$/month in July to 882 g/m$^2$/month in January. It is also worth noting that the performance gap between tracking strategies is highly seasonal and most pronounced during the peak summer months. In Cairo, for instance, the yield difference between dual axis and single axis configurations reaches approximately 350 g/m$^2$/month in July, and 157 g/m$^2$/month in January.

In contrast to this prevailing trend, Dunhuang in Fig. 7**(d)** stands out as a distinctive exception. Under the dual axis tracking configuration, its production profile remains comparatively uniform, fluctuating within a

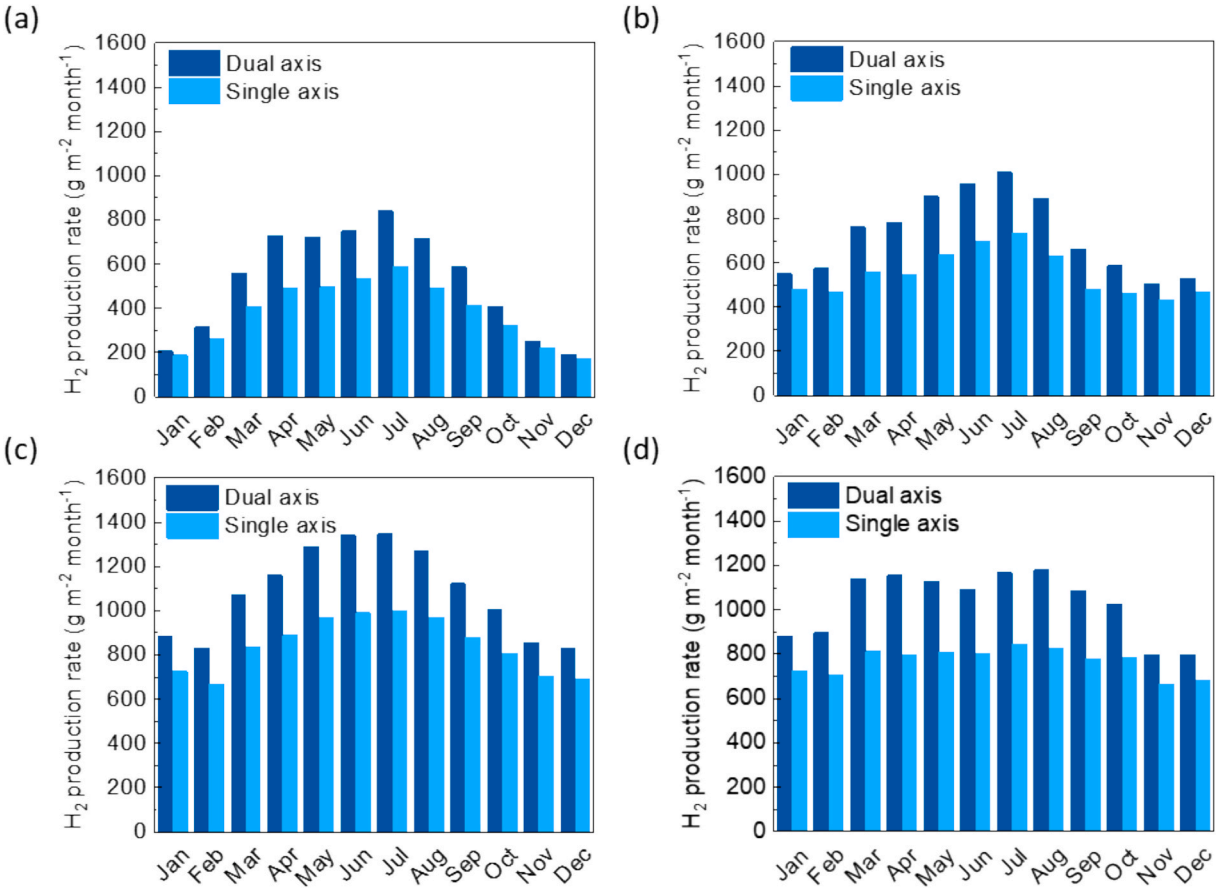


**Fig. 7.** Monthly hydrogen production rates across the four study sites: (a-d) Karlsruhe, Barcelona, Cairo, and Dunhuang. Dark blue bars represent the dual axis tracking system, while light blue bars represent the single axis tracking system.

relatively narrow range between 900 and 1,200 g $m^{-2}$ $month^{-1}$ throughout the year. This seasonal uniformity, which is more pronounced than at the other three sites, may reduce the seasonal mismatch between hydrogen production and demand and consequently lower the required seasonal buffer-storage capacity. The comparison between the tracking modes in Fig. 7**(d)** further underscores the mechanism behind this stability: while the single axis configuration still exhibits a winter decrease similar to those observed at the other sites, the dual axis mechanism more effectively compensates for the lower solar elevation, increasing winter production toward the summer level. Because the principal solar-to-hydrogen conversion process is not supported by grid electricity, the seasonal reductions observed in Karlsruhe, Barcelona, and Cairo directly reduce the corresponding hydrogen-production rates. Dunhuang's distinctive "winter-strong" DNI profile therefore provides an important advantage in reducing seasonal production variability. Nevertheless, continuous hydrogen delivery to downstream industrial processes would still require integration with suitable buffer storage and existing or separately designed hydrogen conditioning and transport infrastructure.

The cumulative impact of these optical and climatic factors is summarized in the annual performance metrics shown in Fig. 8**.** This macroscopic evaluation serves as the definitive indicator of technical feasibility. Under the dual axis configuration in Fig. 8**(a)**, the system Dunhuang achieves an impressive annual hydrogen yield exceeding 12.3 $kg/m^2$, and in Cairo even 13.0 $kg/m^2$. This figure represents a near two-fold increase compared to Karlsruhe of 6.3 $kg/m^2$, quantitatively reinforcing the premise that geographical site selection is a dominant driver of system productivity. In terms of energy conversion, the system achieves a peak annual STH efficiency of 20.0% in Cairo. This high value validates the effectiveness of the proposed spectral-splitting and thermal-integration strategy in minimizing thermodynamic losses. Notably, robust system level annual STH efficiencies were consistently recorded across all four sites, underscoring the universal efficacy of the spectral-splitting approach in enhancing hydrogen production. Furthermore, a clear positive correlation exists between solar resource quality and conversion efficiency: as the site irradiance increases, along with the increase of ambient temperature, the annual STH efficiency rises correspondingly. This trend is attributed to a synergistic thermal-electric coupling where higher irradiance not only maximizes the photovoltaic power output for hydrogen generation but also elevates the operating temperature of the thermally integrated electrolyzer. The resulting higher temperature reduces the electrochemical overpotential required for water splitting, thereby improving the intrinsic efficiency of the electrolysis process.

A direct comparison between Fig. 8**(a) and 8(b)** reveals the substantial efficiency penalty incurred by simplifying the tracking mechanism from two axis to one axis tracking. Transitioning from two axis to single axis tracking causes the annual STH efficiency in Cairo to drop from 20.0% to 15.6%. This decline occurs because the single axis system captures less direct solar energy per unit aperture area, thereby reducing the capacity utilization of the high-efficiency components. Consequently, the significant reduction in specific yield and annual efficiency confirms that high-precision dual axis tracking remains the thermodynamic optimum for concentrating hydrogen systems. Whether the reduced initial hardware CAPEX of single axis trackers can effectively offset these performance penalties to yield a lower LCOH will be rigorously evaluated in the subsequent economic analysis.

### *4.2. Benchmarking the monthly average daily profile method against hourly TMY method*

To quantify the potential deviation introduced by the reduced temporal resolution of the monthly average daily profile method, its predicted hydrogen production was compared with the results obtained from the 8760-hour hourly TMY method. Identical system configurations, tracking models, operating thresholds, and normalization procedures were applied in both calculations, ensuring that the observed differences originated exclusively from the meteorological temporal resolution. This comparison focuses exclusively on the technical hydrogen-production performance.

Fig. 9 presents the hourly normalized hydrogen production calculated using the hourly TMY method for Karlsruhe and Cairo under the dual axis and single axis configurations. The Karlsruhe profiles exhibit pronounced intermittency and seasonal variability, with frequent low-production periods resulting from the highly variable solar resource. In contrast, Cairo maintains a comparatively regular and consistently high daytime production profile throughout the year. In both locations, the dual axis configuration generally produces more hydrogen than the single axis configuration because it reduces incidence-angle losses and maintains a higher effective irradiance over a broader portion of the day. Periods with zero hydrogen production correspond primarily to nighttime hours or conditions in which the available irradiance falls below the system operating threshold.

The annual normalized hydrogen yields calculated using the monthly average daily profile method and hourly TMY method are compared in Fig. 10. Under the dual axis configuration, the monthly average daily profile method and hourly TMY method predict annual normalized hydrogen yields of 6.3 and 6.8 kg $H_2$ $m^{-2}$ $year^{-1}$ in Karlsruhe, 8.7 and 9.2 kg $H_2$ $m^{-2}$ $year^{-1}$ in Barcelona, 13.0 and 13.1 kg $H_2$ $m^{-2}$ $year^{-1}$ in Cairo, and 12.3 and 12.8 kg $H_2$ $m^{-2}$ $year^{-1}$ in Dunhuang, respectively. Relative to the monthly average daily profile method results, the corresponding hourly TMY method results are higher by 8.4%, 6.0%, 1.0%, and 3.5%, respectively. Under the single axis configuration, the two methods predict annual normalized hydrogen yields of 4.6 and 4.9 kg $H_2$

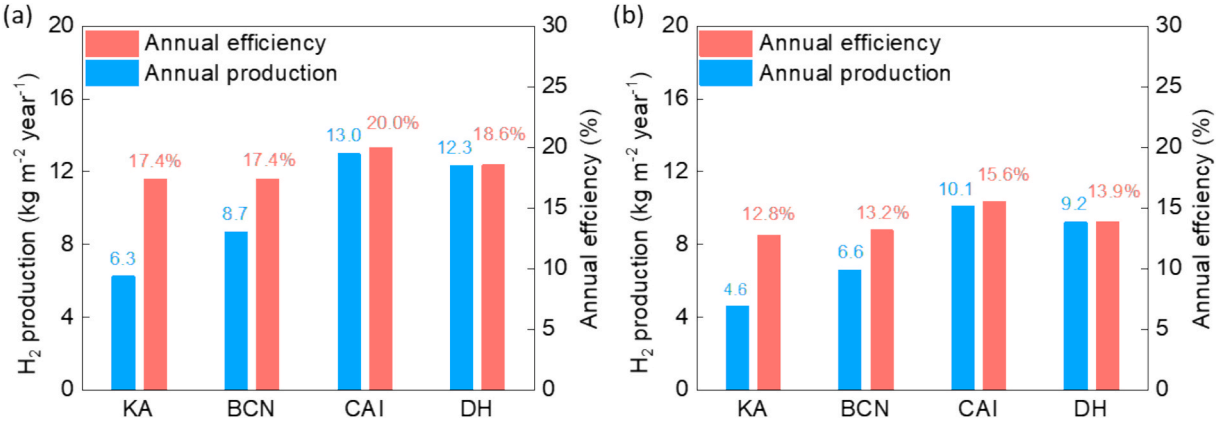


**Fig. 8.** Annual performance summary comparing (a) dual axis tracking and (b) single axis tracking configurations across the four study sites. The blue bars represent the total annual hydrogen production per unit aperture area, while the red bars indicate the annual solar-to-hydrogen STH efficiency.

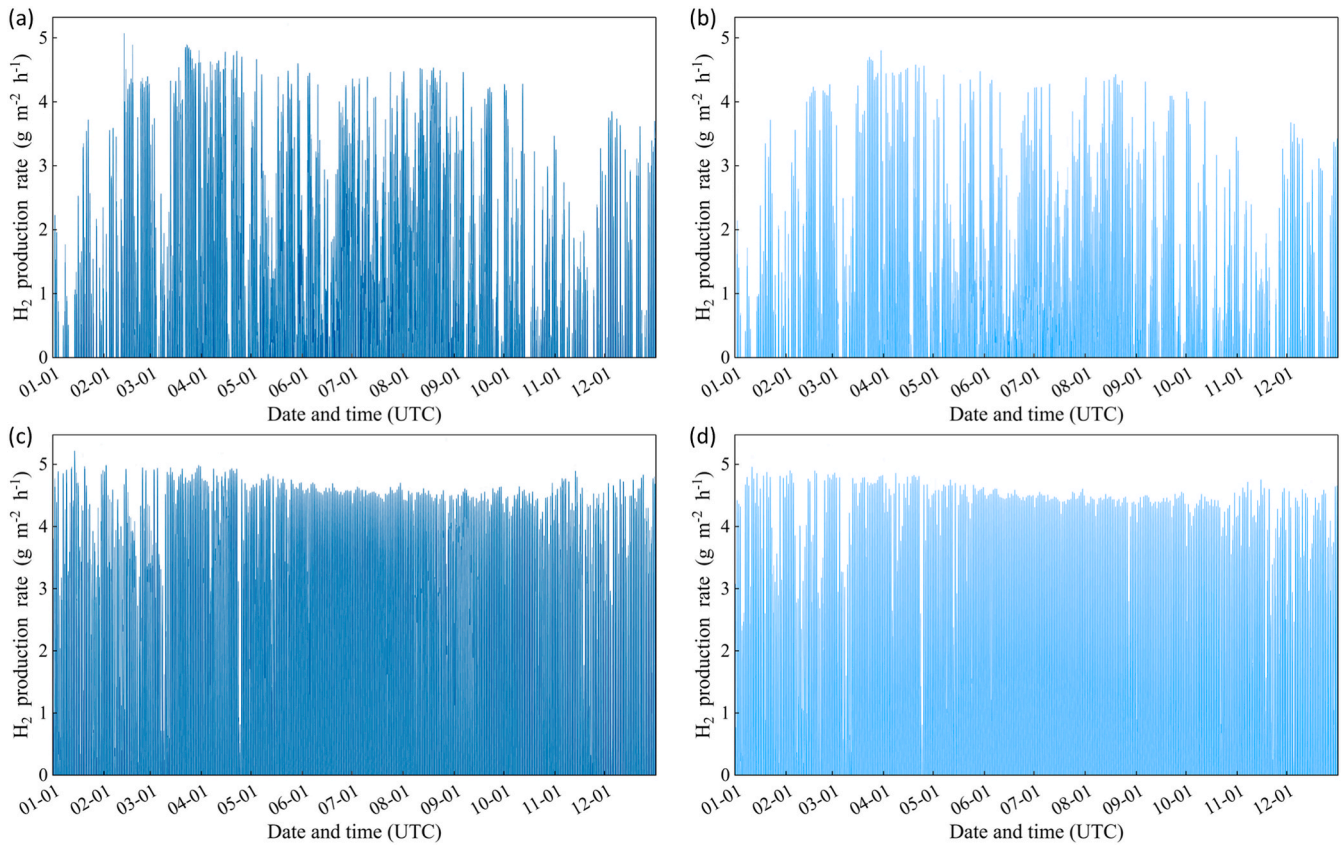


**Fig. 9.** Hourly normalized hydrogen production calculated using 8760-hour hourly TMY method for (a) the dual axis in Karlsruhe, (b) the single axis in Karlsruhe, (c) the dual axis in Cairo, and (d) the single axis in Cairo.

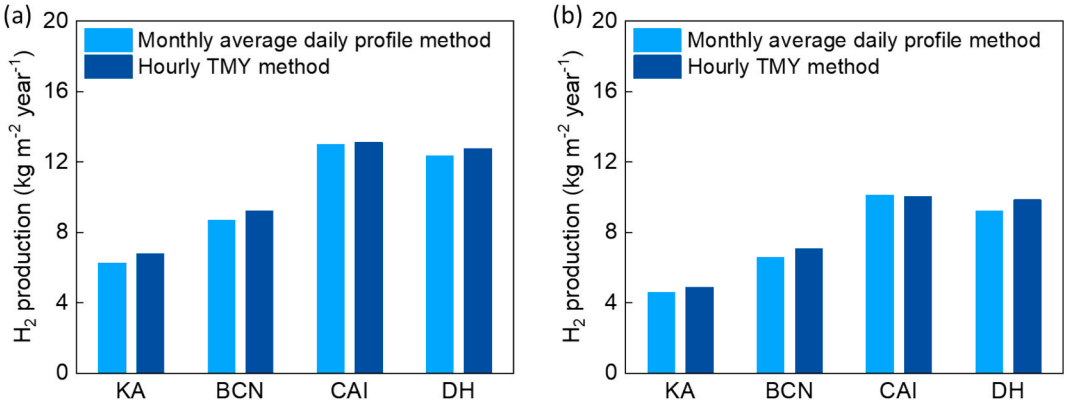


**Fig. 10.** Comparison of annual normalized hydrogen production calculated using monthly average daily profile method and 8760-hour hourly TMY method under (a) dual axis and (b) single axis tracking configurations.

$m^{-2}$ $year^{-1}$ in Karlsruhe, 6.6 and 7.1 kg $H_2$ $m^{-2}$ $year^{-1}$ in Barcelona, 10.1 and 10.0 kg $H_2$ $m^{-2}$ $year^{-1}$ in Cairo, and 9.2 and 9.9 kg $H_2$ $m^{-2}$ $year^{-1}$ in Dunhuang, respectively. The corresponding differences between the hourly TMY method and monthly average daily profile method results are +6.4%, +7.5%, −1.0%, and +6.8%. Thus, the hourly TMY method predicts a slightly higher annual yield in seven of the eight site–tracking combinations, with Cairo under the single axis configuration being the only exception.

The absolute differences between the two methods remain below 8.4% for all locations and tracking configurations, and the average difference is 5.1%. More importantly, both methods produce the same geographical ranking and the same overall comparison between the two tracking strategies: Cairo and Dunhuang achieve the highest annual yields, whereas Karlsruhe exhibits the lowest productivity, and the dual axis configuration consistently outperforms the single axis configuration. The generally higher yields by hourly TMY method can be attributed to the preservation of short-term irradiance variability. Because the system response to irradiance is nonlinear and hydrogen production is suspended below the 45 W $m^{-2}$ operating threshold, the hydrogen yield calculated from an averaged irradiance profile is not necessarily identical to the average yield calculated from the original hourly irradiance values.

Overall, the comparison demonstrates that the simplified monthly average daily profile method provides a reasonable approximation of the annual hydrogen yield and reliably reproduces the principal geographical and tracking-related conclusions of the full-hourly

simulations. The hourly TMY method more accurately captures hourly intermittency, extreme irradiance conditions, and the temporal distribution of hydrogen production. It is therefore more suitable for analyses involving short-term variability, storage requirements, or operational scheduling. It should also be noted that the computational time required by the monthly average daily profile method is only 3.3% of that required by the hourly TMY method, resulting in substantial computational savings. Given the demonstrated accuracy and significantly reduced computational cost of the monthly average daily profile method, the subsequent economic analyses continue to use it.

### 4.3. Economic assessment and sensitivity analysis

Building upon the physical performance metrics, the economic viability of the SSPVTH system is evaluated through the LCOH. The comprehensive cost breakdown across the four study sites is shown in Fig. 11, decomposing the LCOH into CAPEX, annual OPEX, and REPL.

A clear geographical dependence is observed in the economic performance. Consistent with the solar-resource gradients discussed in Section 4.1, the LCOH generally decreases with increasing DNI availability. Under the dual axis configuration **in** Fig. 11**(a)**, the LCOH decreases from 12.3 €/kg in Karlsruhe to 8.9 €/kg in Barcelona, 6.0 €/kg in Cairo, and 6.3 €/kg in Dunhuang. The 51.7% reduction from Karlsruhe to Cairo quantitatively demonstrates the importance of high-DNI site selection in reducing hydrogen production costs. The cost breakdown further shows that CAPEX remains the dominant LCOH component, accounting for approximately 69% of the total LCOH under the dual axis configuration and 72% under the single axis configuration across all sites. These results indicate that the system economics are governed primarily by the initial capital investment and the cumulative hydrogen production over the project lifetime.

A comparison between Fig. 11**(a)** and Fig. 11**(b)** further clarifies the trade-off between tracker cost and hydrogen yield. In Cairo, switching from dual axis to single axis tracking increases the LCOH from 6.0 to 6.6 €/kg, corresponding to an increase of approximately 10.6%. Although the single axis configuration reduces the initial CAPEX from 3,405.6 to 3,073.0 €, representing a cost reduction of approximately 9.8%, its annual hydrogen production decreases from 13.0 to 10. 1 kg $m^{-2}$ $year^{-1}$ a reduction of approximately 22.3%. Therefore, the reduction in hydrogen production is substantially greater than the corresponding saving in initial investment. As a result, the dual axis configuration achieves an LCOH that is 9.6% lower than that of the single axis configuration in Cairo. Its greater annual solar-energy capture increases the lifetime hydrogen output over which the fixed capital costs are distributed, thereby compensating for the additional tracker investment.

To assess the robustness of these economic projections against market uncertainties, a deterministic sensitivity analysis was conducted. The tornado plots in Fig. 12 show the absolute impact on LCOH resulting from a ±10% variation in key techno-economic parameters. A consistent overall hierarchy of influence is observed across all four sites. Macroeconomic factors, specifically the discount rate and inflation, emerge as the dominant drivers of hydrogen cost, generally exerting a stronger influence than individual hardware components. For instance, in Karlsruhe in Fig. 12**(a)**, the ±10% variation in the discount rate results in a ΔLCOH of 0.7 €/kg for the single axis configuration and 0.6 €/kg for the dual axis configuration. The corresponding ΔLCOH values associated with the PV price are 0.3 and 0.2 €/kg, respectively, while those associated with the EC price are 0.5 and 0.4 €/kg. These results underscore the highly capital-intensive nature of the SSPVTH system, for which the cost of capital has a greater influence than the cost of any individual hardware component.

Regarding the hardware parameters, the analysis reveals a distinct sensitivity profile for the tracking mechanisms. As expected, the dual axis configuration shows a higher sensitivity to tracker-price fluctuations than the single axis baseline. This is evident from the wider spread of the dual axis bars for the "Tracker price" parameter in Fig. 12, reflecting the larger portion of CAPEX allocated to the precision mechanical structures. However, even for the dual axis system, the sensitivity to tracker cost remains secondary to the financial parameters. Furthermore, the absolute magnitude of the LCOH variation decreases significantly in high-irradiance regions. For Dunhuang in Fig. 12**(d)**, the absolute impact of all parameters is smaller than that observed for Karlsruhe in Fig. 12**(a)**, indicating that systems deployed in high-irradiance regions are not only cheaper but also exhibit lower absolute LCOH exposure to the same percentage variations in the examined economic inputs.

To provide a comprehensive risk profile that accounts for simultaneous variations in all economic and technical parameters, a Monte Carlo simulation was conducted. The resulting PDFs of the LCOH for the four sites are shown in Fig. 13. These distributions offer a statistical validation of the economic superiority of the dual axis configuration. Across all locations, the probability curve for the dual axis system is consistently shifted to the left relative to the single axis baseline, with a lower P50 (median) value. In Karlsruhe, the dual axis LCOH distribution is between 9 to 18 €/kg, and the P50 is 13.1 €/kg. In Barcelona, the distribution range is narrower, between 7 to 13€/kg, and with a P50 of 9.5 €/kg. In contrast, the single axis P50 for Karlsruhe is 15.5 €/kg and 10.8 €/kg for Barcelona. In Cairo and Dunhuang, the dual axis LCOH distribution is between 4-9 €/kg for both, and P50 at 6.3 €/kg for Cairo and at 6.7 €/kg for Dunhuang. More notably, the peak probability densities of both distribution exceeding 0.6, demonstrating more robust economic performance. This separation indicates that the cost advantage of dual axis tracking is not merely a deterministic outcome of specific base-case assumptions but a statistically robust conclusion that

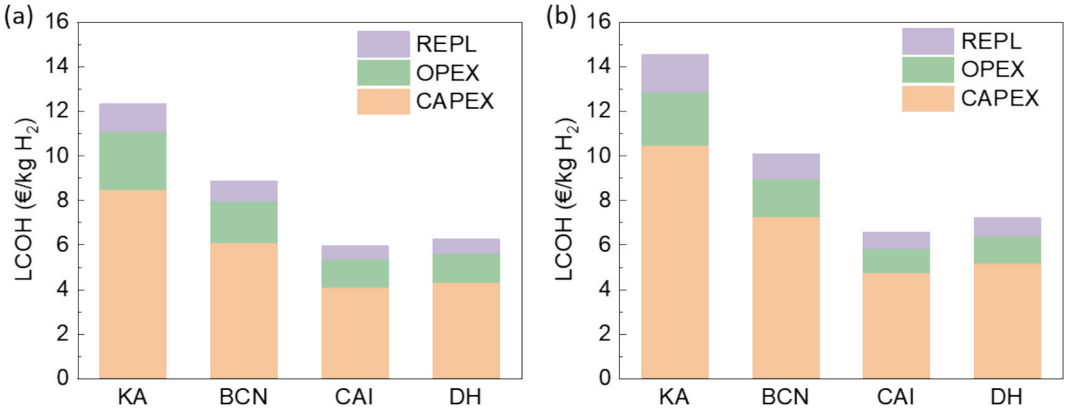


**Fig. 11.** LCOH breakdown by site and tracking configuration: (a) dual axis tracking, and (b) single axis tracking. The cost is decomposed into CAPEX, OPEX, and REPL.

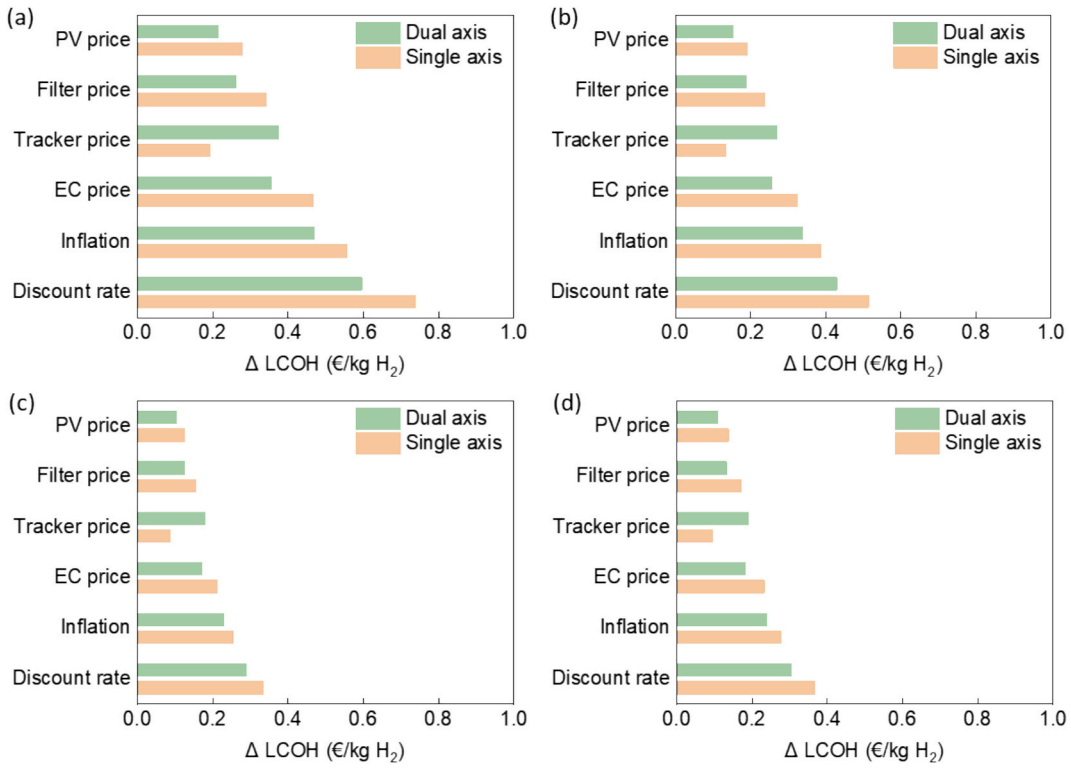


**Fig. 12.** Sensitivity analysis of the LCOH for the four study sites: (a) Karlsruhe, (b) Barcelona, (c) Cairo, and (d) Dunhuang. The charts display the absolute change in LCOH resulting from a uniform ± 10 % variation in each economic and technical parameter. The results highlight that macroeconomic factors, discount rate and inflation, exert a stronger influence on the final cost than the hardware costs of the high-concentration components.

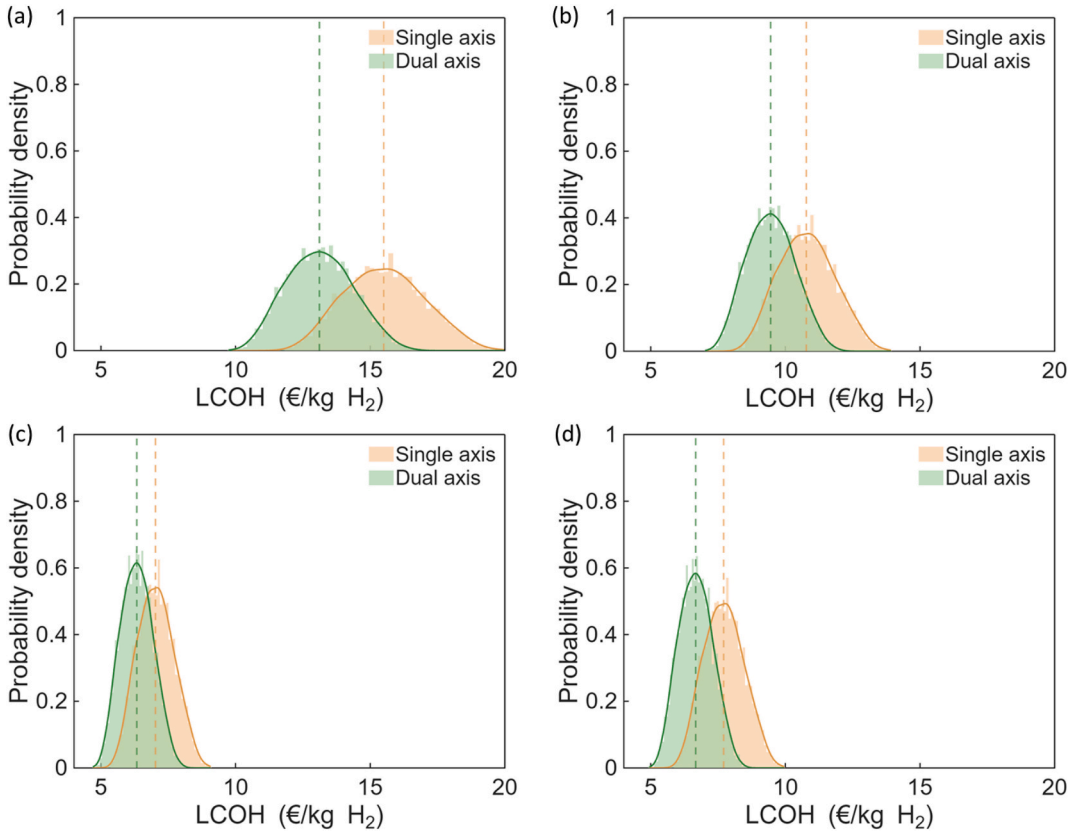


**Fig. 13.** PDFs of the LCOH for (a) Karlsruhe, (b) Barcelona, (c) Cairo, and (d) Dunhuang, derived from a Monte Carlo simulation considering simultaneous uncertainties in economic and technical parameters. The vertical dashed lines indicate the P50 (median) LCOH values. The results demonstrate that dual axis tracking consistently offers a lower cost probability profile and that high-irradiance sites exhibit narrower distributions, indicating lower investment risk.

holds true under a wide range of combined uncertainties. Moreover, the probability density at the P50 median for the dual axis configuration is consistently higher than that of the single axis baseline across all sites. This taller peak implies a significantly narrower distribution variance, suggesting that the dual axis system offers greater statistical certainty and economic robustness compared to the single axis alternative.

Furthermore, the shape of the distributions reveals a critical insight regarding investment risk. The bandwidth of the probability curves narrows significantly as the analysis moves from temperate to arid climates. Karlsruhe in Fig. 13**(a)** exhibits a broad, flattened distribution, implying a high standard deviation and, consequently, greater uncertainty in the final project return. In contrast, Cairo in Fig. 13 **(c)** and Dunhuang in Fig. 13**(d)** presents a sharp, narrow peak. This concentrated distribution suggests that high-irradiance sites offer not only lower costs but also higher financial predictability, as the overwhelming abundance of solar resource acts as a buffer against market and supply chain volatilities. A quantitative comparison further reinforces this geographical dominance: as shown in Fig. 13**(c) and 13(d)**, the P95 (worst-case) LCOH values for Cairo and Dunhuang hover around 7.3 €/kg and 7.7 €/kg. Remarkably, this value remains lower than the P5 (best-case) value for Karlsruhe, at 11.2 €/kg in Fig. 13 **(a)**. This stark contrast demonstrates that even under the most adverse combination of economic and technical uncertainties, the hydrogen production cost in high-irradiance regions remains superior to the most optimistic scenarios achievable in temperate zones. Therefore, from the perspective of risk management, deploying dual axis systems in high-DNI regions represents the strategy with the highest probability of minimizing LCOH while maximizing investment security. The Monte Carlo-derived P5, P50, and P95 values for all locations and tracking configurations are summarized in Table 3. The P50 values are slightly higher than the corresponding deterministic LCOH results. For example, under the Cairo dual axis configuration, the deterministic LCOH is 6.0 € $kg^{-1}$, whereas the Monte Carlo P50 is 6.3 € $kg^{-1}$. This difference is primarily attributable to the real-discount-rate distribution adopted in the Monte Carlo analysis. The deterministic calculation uses a real discount rate of 4.0%, whereas the uniform uncertainty range of 3.0%–7.0% has a midpoint of 5.0%. Together with the inflation rate of 2.0%, these values correspond to nominal discount rates of approximately 6.1% and 7.1%, respectively. The higher central discount rate in the Monte Carlo analysis therefore shifts the LCOH distribution upward. In addition, because the LCOH is calculated from discounted cash flows using nonlinear functions of the sampled component costs and financial parameters, the median LCOH obtained from simultaneous Monte Carlo sampling is not necessarily identical to the LCOH evaluated using the deterministic base-case parameters. Thus, the observed difference is mainly caused by the assumed real-discount-rate distribution, while the nonlinear LCOH calculation provides a smaller additional contribution.

The final dimension of the economic evaluation focuses on the PBT, a critical metric for assessing financial liquidity and investment risk. The capital recovery period across the four sites under two distinct revenue scenarios are compared in Fig. 14: a baseline scenario considering only hydrogen sales in Fig. 14**(a)** and an enhanced scenario that includes the commercial valorization of the oxygen byproduct in Fig. 14**(b)**. Under the baseline hydrogen-only scenario, the geographical disparity is evident. In the low-irradiance region of Karlsruhe, the PBT is approximately 17 years for the dual axis system and 26 years for the single axis system. The latter exceeds the assumed 25-year project lifetime, indicating that the initial investment in the single axis system is not recovered within its operational lifetime. Conversely, the high-irradiance sites of Cairo and Dunhuang demonstrate strong financial viability, with PBT values of approximately 6 years for the dual axis configuration. This confirms that, even without accounting for secondary revenue streams, the high specific hydrogen yield in high-irradiance climates enables relatively rapid capital recovery.

The integration of oxygen sales in Fig. 14**(b)** serves as an economic accelerator. Monetizing the oxygen byproduct creates an additional revenue stream that effectively shortens the payback period across all locations. For the prime site of Cairo, this valorization strategy reduces the PBT from 6 years to approximately 5 years under the dual axis configuration. A 5-year payback period for a renewable energy infrastructure project represents an exceptionally high level of profitability, significantly lowering the barrier for commercial adoption. The impact of oxygen valorization is even more pronounced for the high-latitude site of Karlsruhe. Here, the inclusion of oxygen sales reduces the PBT from 17 to 15 years for the dual axis system and from 26 to 21 years for the single axis system, corresponding to reductions of 2 and 5 years, respectively. This substantial reduction highlights a critical economic dynamic: while high-irradiance sites benefit from oxygen sales as an accelerator to further boost profitability, low-irradiance sites rely on such secondary revenue streams as a vital lever to mitigate their inherent geographical disadvantages and improve project viability. In every case, the dual axis system achieves capital recovery faster than the single axis alternative, proving that the incremental revenue from maximized production far outweighs the additional upfront cost of the tracking hardware. Consequently, the combination of high-irradiance site selection, dual axis tracking technology, and byproduct valorization emerges as the optimal pathway to achieve the shortest capital recovery and highest economic resilience.

Because the PBT depends directly on the assumed product revenues, an additional sensitivity analysis is performed to evaluate the robustness of the base-case hydrogen selling price of 12.0 € $kg^{-1}$. The hydrogen selling price was varied by ±20%, corresponding to 9.6, 12.0, and 14.4 € $kg^{-1}$. For the combined hydrogen-and-oxygen revenue scenario, the oxygen selling price was also varied by ±20%, from 0.12 to 0.18 € $kg^{-1}$ around its base value of 0.15 € $kg^{-1}$. The resulting changes in PBT are presented in Fig. 15. The results reveal that the hydrogen selling price has a substantially greater influence on the PBT than the oxygen selling price. Moreover, the PBT response is asymmetric: the increase caused by a 20% price reduction is generally larger than the decrease achieved by a 20% price increase. This effect is particularly pronounced in Karlsruhe. When the hydrogen selling price decreases from 12.0 to 9.6 € $kg^{-1}$, the PBT under the combined revenue scenario increases from 14.5 to 22.3 years for the dual axis configuration and from 21.0 to 34.4 years for the single axis configuration. The latter exceeds the assumed 25-year system lifetime, indicating limited economic robustness under the lower-price scenario. In comparison, Cairo and Dunhuang remain considerably less sensitive to the hydrogen price reduction. At 9.6 € $kg^{-1}$, the PBT values are 6.2 and 7.3 years in Cairo and 6.7 and 8.2 years in Dunhuang for the dual axis and single axis configurations, respectively. Barcelona exhibits intermediate PBT values of 11.9 and 14.7 years. These results demonstrate that the dual axis configuration retains a shorter PBT than the single axis configuration throughout the investigated selling-price range. However, they also indicate that the economic robustness of the system depends strongly on the available solar resource: high-irradiance locations remain financially viable under a reduced

**Table 3**
Monte Carlo uncertainty results for levelized cost of hydrogen at different locations and tracking configurations.

| Site | Tracker | LCOH_P5 (€/kg) | LCOH_P50 (€/kg) | LCOH_P95 (€/kg) |
|---|---|---|---|---|
| Karlsruhe | Single axis | 13.2 | 15.5 | 18.1 |
| | Dual axis | 11.2 | 13.1 | 15.2 |
| Barcelona | Single axis | 9.2 | 10.8 | 12.5 |
| | Dual axis | 8.1 | 9.5 | 11.0 |
| Cairo | Single axis | 6.0 | 7.0 | 8.2 |
| | Dual axis | 5.4 | 6.3 | 7.3 |
| Dunhuang | Single axis | 6.5 | 7.7 | 9.0 |
| | Dual axis | 5.7 | 6.7 | 7.7 |

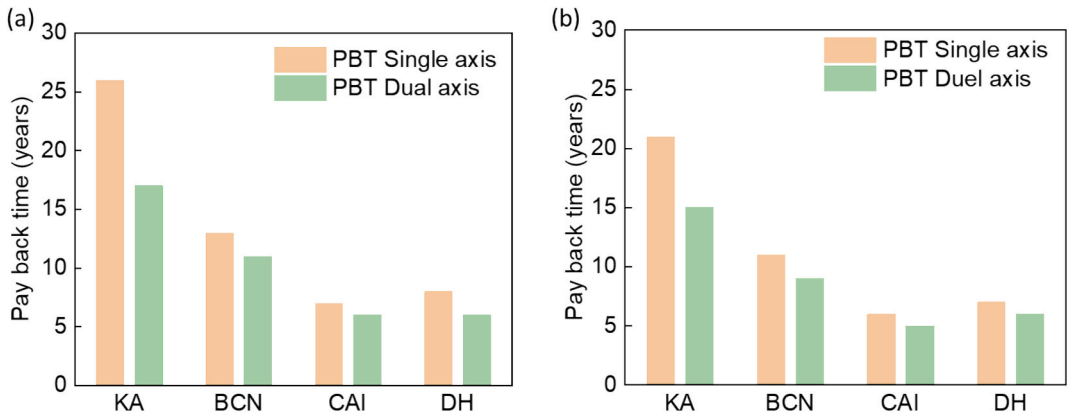


**Fig. 14.** PBT for the four study sites under two economic scenarios: (a) hydrogen sales only, and (b) hydrogen and oxygen sales. The results demonstrate that oxygen byproduct valorization generally accelerates capital recovery across the investigated sites and tracking configurations. Under the dual axis configuration, the PBT decreases from 6 to 5 years in Cairo, while it remains 6 years in Dunhuang when reported at annual resolution.

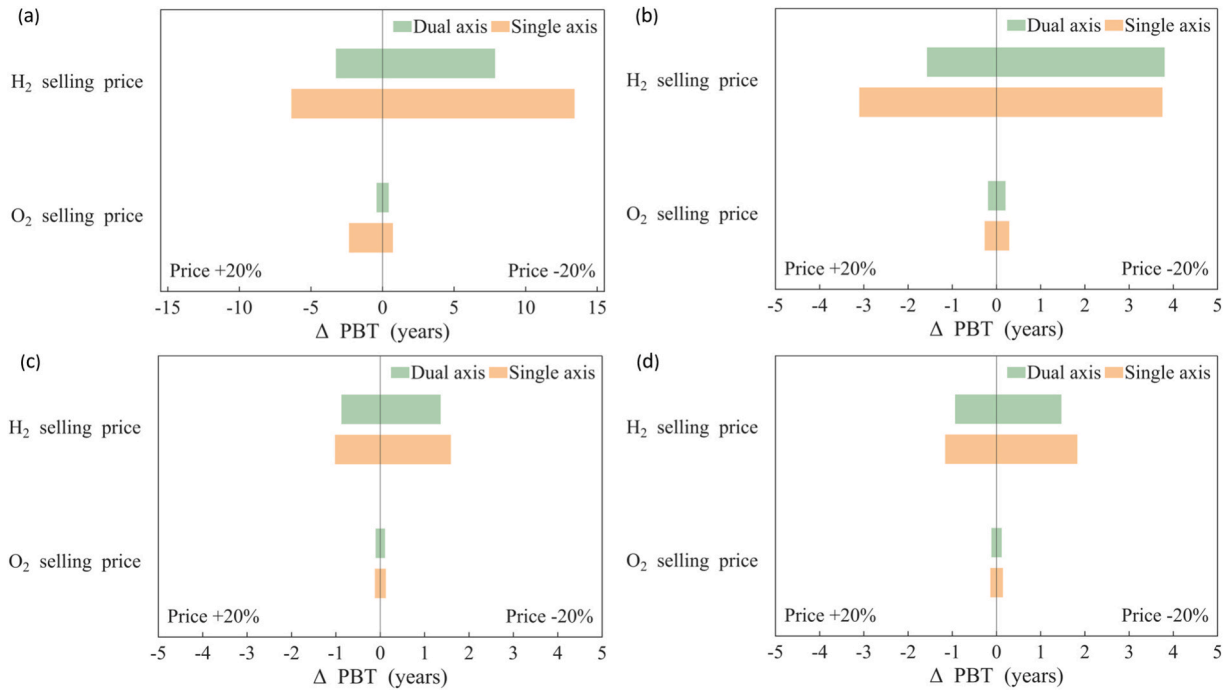


**Fig. 15.** Effects of ± 20 % variations in $H_2$ and $O_2$ selling prices on the PBT of the dual axis and single axis solar tracking configurations in: (a) Karlsruhe, (b) Barcelona, (c) Cairo, and (d) Dunhuang. ΔPBT represents the change relative to the corresponding baseline PBT; negative and positive values indicate shortened and extended payback periods, respectively.

hydrogen selling price, whereas low-irradiance locations are substantially more exposed to future hydrogen-price reductions.

To examine the potential influence of long-term performance losses on the economic results, a system-level degradation sensitivity analysis was conducted in addition to the established base-case assessment. The no-degradation condition was retained as the reference scenario, while annual performance degradation rates of 0.5%, 1.0%, 1.5%, and 2.0% were introduced to quantify their effects on the LCOH and PBT. The same degradation multiplier was applied to the annual hydrogen production and the corresponding oxygen byproduct. Consistent with the scheduled replacement expenditure assumed every 10 years, the accumulated degradation was reset following each replacement event. Therefore, the system output was restored at the beginning of years 11 and 21. All other technical and economic parameters were held constant.

Fig. 16 shows the resulting influence on the LCOH. As expected, the LCOH increases monotonically with the annual degradation rate because the discounted lifetime hydrogen production decreases while the CAPEX, OPEX, and scheduled replacement costs remain unchanged. Taking the 0% degradation case as the reference, the four nonzero annual degradation scenarios of 0.5%, 1.0%, 1.5%, and 2.0% increase the LCOH by approximately 1.9%, 3.9%, 5.8%, and 7.8%, respectively. At an annual degradation rate of 2.0%, the LCOH of dual axis tracking systems increases from 12.3 to 13.3 € $kg^{-1}$ in Karlsruhe, from 8.9 to 9.6 € $kg^{-1}$ in Barcelona, from 6.0 to 6.4 € $kg^{-1}$ in Cairo, and from 6.3 to 6.8 € $kg^{-1}$ in Dunhuang. Under the single axis solar tracking configuration, the corresponding values increase from 14.5 to 15.7 € $kg^{-1}$, from 10.1 to 10.9 € $kg^{-1}$, from 6.6 to 7.1 € $kg^{-1}$, and from 7.2 to 7.8 € $kg^{-1}$, respectively. Although degradation increases the LCOH in every case, the geographical ranking and the economic advantage of the dual axis configuration remain unchanged.

The influence of degradation on the discounted PBT is presented in

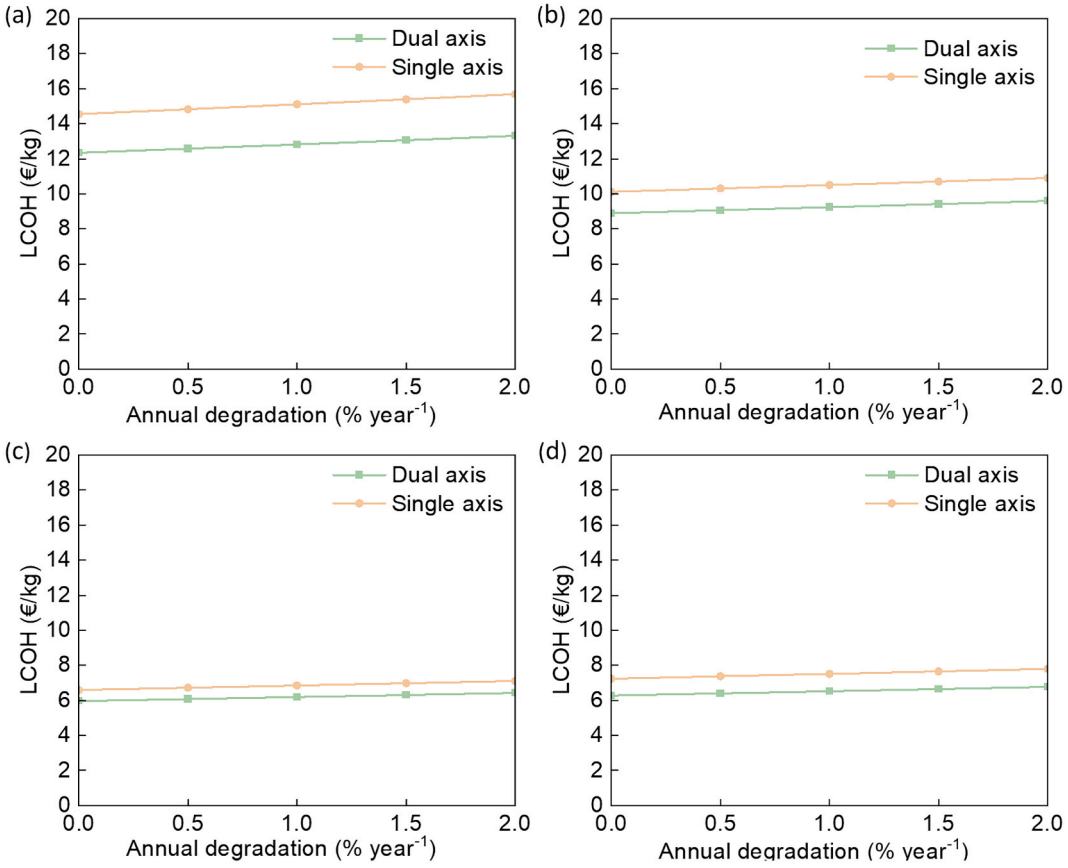


**Fig. 16.** Effects of annual hydrogen-output degradation rates ranging from 0 % to 2 % year$^{-1}$ on the LCOH of the dual axis and single axis solar tracking configurations in (a) Karlsruhe, (b) Barcelona, (c) Cairo, and (d) Dunhuang. Accumulated degradation was reset after each scheduled 10-year replacement cycle.

Fig. 17. The effect is most pronounced in Karlsruhe because its lower annual hydrogen production provides a smaller revenue margin to compensate for degradation-induced production losses. At an annual degradation rate of 2.0%, the hydrogen-only PBT in Karlsruhe increases from 16.9 to 21.2 years for the dual axis configuration and from 25.2 to 32.3 years for the single axis configuration. When oxygen revenue is included, the corresponding PBT values increase from 14.5 to 16.3 years and from 21.0 to 24.3 years, respectively. In comparison, the high-irradiance sites remain substantially less sensitive to degradation. At the same annual degradation rate of 2.0%, the PBT under the combined hydrogen-and-oxygen revenue scenario increases from 4.9 to 5.1 years in Cairo and from 5.2 to 5.5 years in Dunhuang under the dual axis configuration. These results indicate that high-productivity sites are more resilient to long-term performance losses, whereas the economic viability of low-irradiance sites, particularly Karlsruhe under the single axis configuration, is considerably more sensitive to degradation.

Overall, the sensitivity analysis confirms that neglecting performance degradation produces moderately optimistic LCOH and PBT estimates. Nevertheless, within the investigated degradation range of 0%–2.0% year$^{-1}$, the main comparative conclusions remain unchanged: the dual axis configuration retains a lower LCOH and shorter PBT than the single axis configuration, while Cairo and Dunhuang remain economically more favourable than Karlsruhe and Barcelona. The results further demonstrate that maintaining long-term system performance is particularly important for projects located in regions with limited solar resources. The present results should be interpreted within the assumed 10-year degradation-reset framework.

## 5. Conclusions

This study presented a comprehensive techno-economic assessment of a solar-driven SSPVTH system across diverse climatic zones. By integrating high-fidelity optical-thermal simulations with a stochastic economic model, the analysis quantified the impact of geographical location, tracking strategy, and byproduct valorization on the system's feasibility.

Geographical resource quality is identified as the primary determinant of system productivity and stability. The system demonstrates a robust peak annual STH efficiency of 20.0% in high-irradiance regions, validating the efficacy of the spectral-splitting approach in minimizing thermodynamic losses. While high-irradiance sites such as Cairo and Dunhuang achieved annual normalized hydrogen yields of 13.0 and 12.3 kg $H_2$ m$^{-2}$ year$^{-1}$, respectively, under the dual axis configuration, approximately twice the value obtained in Karlsruhe, the temporal profile of production proved equally critical. Dunhuang exhibited a unique "winter-strong" phenomenon, where low ambient temperatures and high winter DNI created a comparatively uniform seasonal production profile. This seasonal uniformity may reduce seasonal buffer-storage requirements, making such climates advantageous for achieving a more balanced hydrogen output throughout the year. Benchmarking against 8760-hour hourly TMY method simulations resulted in differences in annual hydrogen production ranging from −1.0% to +8.4% relative to the monthly average daily profile method, while preserving the geographical ranking of the sites and the relative advantage of dual axis tracking. This agreement supports the robustness of the main technical conclusions against the meteorological temporal resolution adopted in the baseline analysis. The present model employs a fixed AM1.5D spectrum scaled by broadband DNI and therefore does not capture site- and time-dependent spectral variations. Although this standardized approach enables consistent comparison across locations and tracking configurations, spectral variability may affect the energy allocated to the PV cells and thermal absorber. Future work should

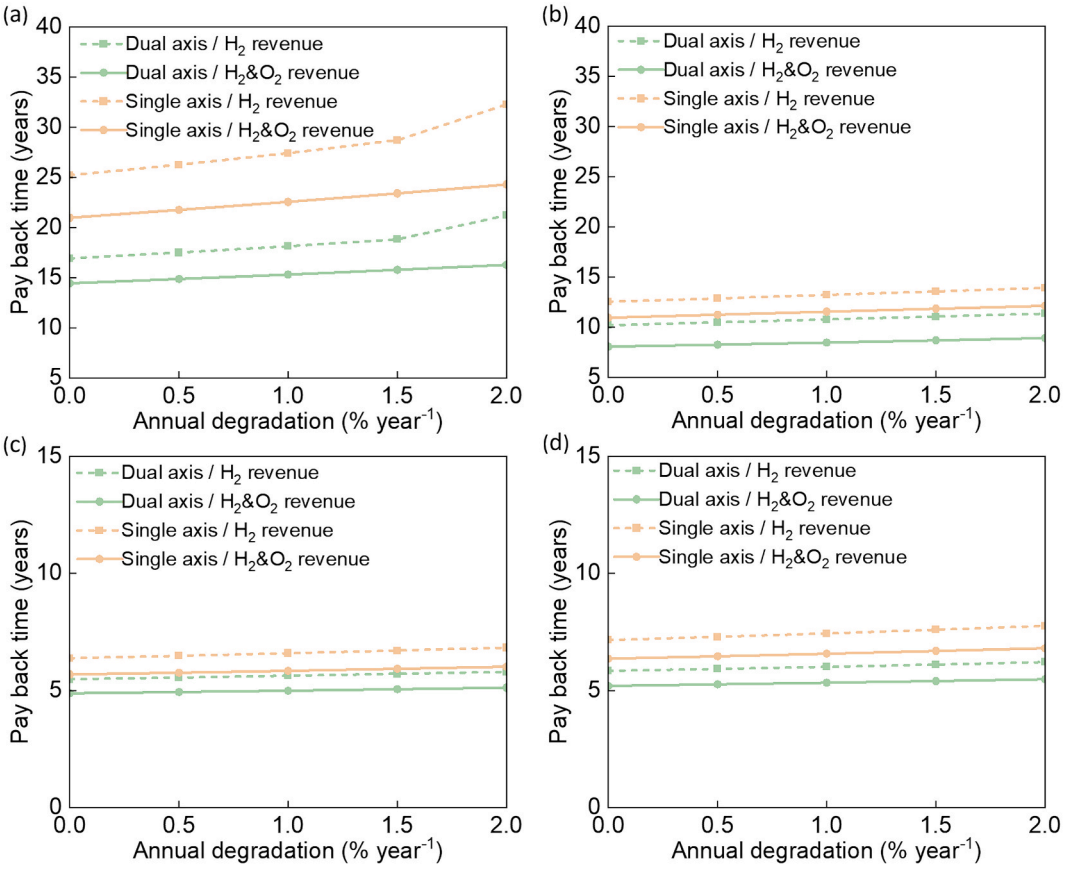


**Fig. 17.** Effects of annual hydrogen-output degradation rates ranging from 0 % to 2 % year$^{-1}$ on the discounted PBT of the dual axis and single axis solar tracking configurations in (a) Karlsruhe, (b) Barcelona, (c) Cairo, and (d) Dunhuang. Dashed lines represent the $H_2$-only revenue scenario, whereas solid lines represent the $H_2$ + $O_2$ revenue scenario. Accumulated degradation was reset after each scheduled 10-year replacement cycle.

incorporate site-specific, time-resolved spectra to quantify their effects on spectral allocation and hydrogen production.

The comparative analysis of tracking mechanisms overturns the conventional wisdom that lower-cost hardware yields lower-cost energy. The results confirm that high-precision dual axis tracking is both the thermodynamic and economic optimum for concentrating hydrogen systems. Although single axis trackers reduce initial CAPEX, the associated optical misalignment and cosine losses cause a disproportionate drop in annual yield (dropping STH efficiency to 15.6% in Cairo). Consequently, the dual axis configuration achieves a lower LCOH of ~6.0 €/kg in prime locations, effectively diluting the high fixed capital costs over a maximized production volume.

The economic sensitivity and risk analysis reveal that the SSPVTH system is highly capital-intensive, with financial viability driven more by macroeconomic parameters than by component hardware costs. Sensitivity analysis indicates that discount rates and inflation exert the strongest influence on LCOH. Monte Carlo simulations further demonstrate that deployment in high-irradiance regions significantly compresses the risk profile, producing a narrower probability distribution of costs. Under the favourable assumptions of full oxygen offtake and no additional downstream conditioning or delivery costs, byproduct valorization can reduce the discounted PBT to approximately 5 years in optimal locations. This result should be interpreted as an optimistic upper bound on the potential economic benefit of oxygen utilization. The selling-price sensitivity analysis further shows that a ±20% variation in the hydrogen selling price has a substantially greater effect on PBT than the same relative variation in the oxygen selling price. The degradation analysis shows that, under the assumed 10-year degradation reset, annual performance degradation rates of 0.5%, 1.0%, 1.5%, and 2.0% increase the LCOH by approximately 1.9%, 3.9%, 5.8%, and 7.8%, respectively, while also extending the PBT. Nevertheless, the geographical ranking of the sites and the economic advantage of dual axis tracking remain unchanged over the investigated degradation range. In conclusion, this work demonstrates that solar-driven SSPVTH technology is technically feasible and economically promising when deployed in regions with high direct normal irradiance. To achieve industrial-grade viability, future project development should prioritize high-DNI sites with favourable winter profiles, adopt dual axis tracking to maximize capacity utilization, and integrate byproduct value chains. These strategies collectively provide a robust pathway toward achieving competitive green hydrogen production in the coming decade.

## CRediT authorship contribution statement

**Yu Tian:** Writing – review & editing, Writing – original draft, Visualization, Methodology, Investigation, Formal analysis, Conceptualization. **Pooria Hadikhani:** Writing – review & editing, Methodology, Formal analysis. **Christos N. Markides:** Writing – review & editing, Formal analysis. **Gan Huang:** Writing – review & editing, Writing – original draft, Visualization, Supervision, Resources, Investigation, Funding acquisition, Formal analysis, Conceptualization.

## Declaration of competing interest

The authors declare that they have no known competing financial interests or personal relationships that could have appeared to influence the work reported in this paper.

## Acknowledgements

This work received support from the: i) Initiative and Networking Fund of the Helmholtz Association under the call Helmholtz Investigator Group (VH-NG-21-07, UNICOS) by G.H.; ii) Research Field Energy: Program Materials and Technologies for the Energy Transition (Topic 1 Photovoltaics and Wind Energy, ref. 38.01.04) by G.H.; and (iii) Karlsruhe School of Optics and Photonics (KSOP) by Y.T. and G.H.. C.N.M. would like to thank UK company Solar Flow Ltd. (www.solar-flow.co.uk). For the purpose of Open Access, the authors have applied a CC BY public copyright license to any Author Accepted Manuscript version arising from this submission.

## Data availability

Data will be made available on request.

## References

[1] Li Z, Fang S, Sun H, Chung RJ, Fang X, He JH. Solar hydrogen Adv Energy Mater 2023;13:2203019. https://doi.org/10.1002/aenm.202203019.
[2] Global Hydrogen Review 2023. 2023 [accessed 5 February 2026], https://www.iea.org/reports/global-hydrogen-review-2023;.
[3] International Renewable Energy Agency (IRENA). Hydrogen, https://www.irena.org/Energy-Transition/Technology/Hydrogen; [accessed 5 February 2026].
[4] Squadrito G, Maggio G, Nicita A. The green hydrogen revolution. Renew. Energy 2023;216:119041. https://doi.org/10.1016/j.renene.2023.119041.
[5] PwC. The green hydrogen cost, https://www.pwc.com/gx/en/industries/energy-utilities-resources/green-hydrogen-cost.html; [accessed 5 February 2026].
[6] U.S. Department of Energy. Hydrogen Shot: Water Electrolysis Technology Assessment, https://www.energy.gov/sites/default/files/2025-06/hydrogen-shot-water-electrolysis-technology-assessment-1.pdf; 2025 [accessed 5 February 2026].
[7] Grube T, Reul J, Reuß M, Calnan S, Monnerie N, Schlatmann R, et al. A techno-economic perspective on solar-to-hydrogen concepts through 2025. Sustain Energy Fuels 2020;4:5818–34.https://doi.org/10.1039/D0SE00896F.
[8] Curcio E. Techno-economic analysis of hydrogen production: costs, policies, and scalability in the transition to net-zero. Int J Hydrog Energy 2025;128:473–87. https://doi.org/10.1016/j.ijhydene.2025.04.013.
[9] International Renewable Energy Agency (IRENA). Green hydrogen cost reduction. ISBN 978-92-9260-295-6. https://www.irena.org/publications/2020/Dec/Green-hydrogen-cost-reduction [accessed 5 February 2026].
[10] Victoria M, Haegel N, Peters IM, Sinton R, Jäger-Waldau A, Del Cañizo C, et al. Solar photovoltaics is ready to power a sustainable future. Joule 2021;5:1041–56. https://doi.org/10.1016/j.joule.2021.03.005.
[11] Herrando M, Wang K, Huang G, Otanicar T, Mousa OB, Agathokleous RA, et al. A review of solar hybrid photovoltaic-thermal (PV-T) collectors and systems. Prog Energy Combust Sci 2023;97:101072. https://doi.org/10.1016/j.pecs.2023.101072.
[12] Huang G, Wang K, Markides CN. Efficiency limits of concentrating spectral-splitting hybrid photovoltaic-thermal (PV-T) solar collectors and systems. Light Sci Appl 2021;10:28. https://doi.org/10.1038/s41377-021-00465-1.
[13] Fallisch A, Schellhase L, Fresko J, Zedda M, Ohlmann J, Steiner M, et al. Hydrogen concentrator demonstrator module with 19.8% solar-to-hydrogen conversion efficiency according to the higher heating value. Int J Hydrogen Energy 2017;42(43):26804–15.
[14] Nakamura A, Ota Y, Koike K, Hidaka Y, Nishioka K, Sugiyama M, et al. A 24.4% solar to hydrogen energy conversion efficiency by combining concentrator photovoltaic modules and electrochemical cells. Appl Phys. Express 2015;8:107101. https://doi.org/10.7567/APEX.8.107101.
[15] Holmes-Gentle I, Tembhurne S, Suter C, Haussener S. Kilowatt-scale solar hydrogen production system using a concentrated integrated photoelectrochemical device. Nat Energy 2023;8:586–96. https://doi.org/10.1038/s41560-023-01247-2.
[16] Li W, Tian H, Ma L, Wang Y, Liu X, Gao X. Low-temperature water electrolysis: fundamentals, progress, and new strategies. Mater Adv 2022;3:5598–644. https://doi.org/10.1039/D2MA00185C.
[17] Bonanno M, Müller K, Bensmann B, Hanke-Rauschenbach R, Aili D, Franken T, et al. Review and prospects of PEM water electrolysis at elevated temperature operation. Adv Mater Technol 2024;9:2300281. https://doi.org/10.1002/admt.202300281.
[18] Huang G, Markides CN. Spectral-splitting hybrid PV-thermal (PV-T) solar collectors employing semi-transparent solar cells as optical filters. Energy Convers Manag 2021;248:114776. https://doi.org/10.1016/j.enconman.2021.114776.
[19] Huang G, Wang K, Curt SR, Franchetti B, Pesmazoglou I, Markides CN. On the performance of concentrating fluid-based spectral-splitting hybrid PV-thermal (PV-T) solar collectors. Renew Energy 2021;174:590–605. https://doi.org/10.1016/j.renene.2021.04.070.
[20] Tian Z, Wang Z, Liu Y, Wu H, Li W, Wei H. Full-spectrum solar hydrogen production enabled by spectral splitting and electro-thermal management. Energy Convers Manag 2026;351:121045. https://doi.org/10.1016/j.enconman.2026.121045.
[21] Li Q, Jiang L, Huang G, Wang DW, Shepherd J, Daiyan R, et al. A ternary system exploiting the full solar spectrum to generate renewable hydrogen from a waste biomass feedstock. Energy Environ Sci 2023;16:3497–513. https://doi.org/10.1039/D3EE00603D.
[22] Pandey C, Wu M, Oyeniran A, Chougule SS, Acosta Pazmiño I, Rivera-Solorio CI, et al. Numerical study of a parabolic-trough CPV-T collector with spectral-splitting liquid filters. Front Energy 2025:1–20. https://doi.org/10.1007/s11708-025-1028-y.
[23] Obalanlege MA, Xu J, Markides CN, Mahmoudi Y. Techno-economic analysis of a hybrid photovoltaic-thermal solar-assisted heat pump system for domestic hot water and power generation. Renew Energy 2022;196:720–36. https://doi.org/10.1016/j.renene.2022.07.044.
[24] Tian Y, Hadikhani P, Alati N, Richards BS, Huang G. Hybrid solar spectral-splitting photovoltaic-thermal hydrogen production systems. Adv Sci 2025. https://doi.org/10.1002/advs.202503205. 2503205.
[25] Hou G, Wang Z, Zhang Y, Kalogirou SA, Markides CN. Experimental and numerical investigation of a PVT-PEM system: impact of flow channel configurations on hydrogen production. Renew. Energy 2026:125741. https://doi.org/10.1016/j.renene.2026.125741.
[26] Hadikhani P, Hashemi SMH, Schenk SA, Psaltis D. A membrane-less electrolyzer with porous walls for high throughput and pure hydrogen production. Sustain Energy Fuels 2021;5:2419–32. https://doi.org/10.1039/D1SE00255D.
[27] Hashemi SMH, Karnakov P, Hadikhani P, Chinello E, Litvinov S, Moser C, et al. A versatile and membrane-less electrochemical reactor for the electrolysis of water and brine. Energy Environ Sci 2019;12:1592–604. https://doi.org/10.1039/C9EE00219G.
[28] Herrando M, Markides CN. Hybrid PV and solar-thermal systems for domestic heat and power provision in the UK: Techno-economic considerations. Appl Energy 2016;161:512–32. https://doi.org/10.1016/j.apenergy.2015.09.025.
[29] Peacock J, Huang G, Song J, Markides CN. Techno-economic assessment of integrated spectral-beam-splitting photovoltaic-thermal (PV-T) and organic Rankine cycle (ORC) systems. Energy Convers Manag 2022;269:116071. https://doi.org/10.1016/j.enconman.2022.116071.
[30] Mostafaeipour A, Rezayat H, Rezaei M. A thorough investigation of solar-powered hydrogen potential and accurate location planning for big cities: a case study. Int J Hydrog Energy 2020;45:31599–611. https://doi.org/10.1016/j.ijhydene.2020.08.211.
[31] Yum SG, Adhikari MD. Suitable site selection for the development of solar based smart hydrogen energy plant in the Gangwon-do region, South Korea using big data: a geospatial approach. Int J Hydrog Energy 2023;48:36295–313. https://doi.org/10.1016/j.ijhydene.2025.03.025.
[32] European Commission Joint Research Centre (JRC). PVGIS: Photovoltaic geographical information system. https://re.jrc.ec.europa.eu/pvg_tools/en/#MR [accessed 6 February 2026].
[33] Duffie JA, Beckman WA. Solar engineering of thermal processes. 4th ed. Hoboken: John Wiley & Sons; 2013. https://doi.org/10.1002/9781118671603.
[34] Jin Q, Zhang Q, Rainer C, Hu H, Chen J, Gehring T, et al. Nat Commun 2024;15:3372. https://doi.org/10.1038/s41467-024-47086-x.
[35] Zhang Q, Jin Q, Mertens A, Rainer C, Huber R, Fessler J, et al. Adv Mater 2022;34:2201348. https://doi.org/10.1002/adma.202201348.
[36] Honsberg CB, Bowden SG. Photovoltaics education website. https://www.pveducation.org [accessed June 2024].
[37] Chaibi Y, Allouhi A, Malvoni M, Salhi M, Saadani R. Solar irradiance and temperature influence on the photovoltaic cell equivalent-circuit models. Sol Energy 2019;188:1102–10. https://doi.org/10.1016/j.solener.2019.07.005.
[38] Silverman TJ, Deceglie MG, Marion B, Cowley S, Kayes B, Kurtz S, et al. IEEE 39th photovoltaic specialists conference (PVSC). IEEE 2013;2013:0103–8. https://doi.org/10.1109/PVSC.2013.6744109.
[39] Dobreva P, van Dyk EE, Vorster FJ. Irradiance and temperature corrections of current-voltage curves—Quintessential nature and implications. Sol Energy 2021;227:116–25. https://doi.org/10.1016/j.solener.2021.08.057.
[40] Lohmann-Richters FP, Renz S, Lehnert W, Müller M, Carmo M. Challenges and opportunities for increased current density in alkaline electrolysis by increasing the operating temperature. J Electrochem Soc 2021;168:114501. https://doi.org/10.1149/1945-7111/ac34cc.
[41] Allebrod F, Chatzichristodoulou C, Mollerup PL, Mogensen MB. Electrical conductivity measurements of aqueous and immobilized potassium hydroxide. Int J Hydrogen Energy 2012;37:16505–14. https://doi.org/10.1016/j.ijhydene.2012.02.088.
[42] Grdeń M, Jerkiewicz G. Influence of surface treatment on the kinetics of the hydrogen evolution reaction on bulk and porous nickel materials. Electrocatalysis 2019;10:173–83. https://doi.org/10.1007/s12678-019-0506-6.
[43] Chanda D, Hnát J, Dobrota AS, Pašti IA, Paidar M, Bouzek K. The effect of surface modification by reduced graphene oxide on the electrocatalytic activity of nickel towards the hydrogen evolution reaction. PCCP 2015;17:26864–74. https://doi.org/10.1039/C5CP04238K.
[44] Miles MH, Kissel G, Lu PWT, Srinivasan S. Effect of temperature on electrode kinetic parameters for hydrogen and oxygen evolution reactions on nickel electrodes in alkaline solutions. J Electrochem Soc 1976;123:332–6. https://doi.org/10.1149/1.2132820.
[45] Guarracino I, Mellor A, Ekins-Daukes NJ, Markides CN. Dynamic coupled thermal-and-electrical modelling of sheet-and-tube hybrid photovoltaic/thermal (PVT) collectors. Appl Therm Eng 2016;101:778–95. https://doi.org/10.1016/j.applthermaleng.2016.02.056.

[46] Notton G, Cristofari C, Mattei M, Poggi P. Modelling of a double-glass photovoltaic module using finite differences. Appl Therm Eng 2005;25:2854–77. https://doi.org/10.1016/j.applthermaleng.2005.02.008.
[47] Herrando M, Markides CN, Hellgardt K. A UK-based assessment of hybrid PV and solar-thermal systems for domestic heating and power: System performance. Appl Energy 2014;122:288–309. https://doi.org/10.1016/j.apenergy.2014.01.061.
[48] The Engineering ToolBox. Water – specific heat capacity. https://www.engineeringtoolbox.com/specific-heat-capacity-water-d_660.html [accessed 5 February 2026].
[49] Chevron. Chevron lubricants: Delo 400 LE SAE 15W-40. https://cglapps.chevron.com/msdspds/PDSDetailPage.aspx?docDataId=77158 [accessed 5 February 2026].
[50] Cui X, Chua KJ, Islam MR, Yang WM. Fundamental formulation of a modified LMTD method to study indirect evaporative heat exchangers. Energy Convers Manag 2014;88:372–81. https://doi.org/10.1016/j.enconman.2014.08.056.
[51] LeRoy RL, Bowen CT, LeRoy DJ. The thermodynamics of aqueous water electrolysis. J Electrochem Soc 1980;127:1954–62. https://doi.org/10.1149/1.2130044.
[52] The Engineering ToolBox. Metals, metallic elements and alloys – thermal conductivities. https://www.engineeringtoolbox.com/thermal-conductivity-metalsd_858.html [accessed 5 February 2026].
[53] Pásztory Z. An overview of factors influencing thermal conductivity of building insulation materials. J Build Eng 2021;44:102604. https://doi.org/10.1016/j.jobe.2021.102604.
[54] Ren Z, Peng Y, Zhu Y, He B, Zeng Z, Liu Q, et al. A climate-tailored predictive methodology for directly coupled photovoltaic-electrolyzer systems. Sol Energy 2026;307:114342. https://doi.org/10.1016/j.solener.2026.114342.
[55] Lee B, Fan D, Forrest SR. A high throughput, linear molecular beam epitaxy system for reduced cost manufacturing of GaAs photovoltaic cells: will GaAs ever be inexpensive enough? Sustain Energy Fuels 2020;4:2035–42. https://doi.org/10.1039/C9SE01255A.
[56] Esposito DV. Membraneless electrolyzers for low-cost hydrogen production in a renewable energy future. Joule 2017;1:651–8. https://doi.org/10.1016/j.joule.2017.07.003.
[57] Abu Dhabi: International Renewable Energy Agency 2020. https://www.irena.org/-/media/Files/IRENA/Agency/Publication/2020/Dec/IRENA_Green_hydrogen_cost_2020.pdf.
[58] Sharma R, Gao H. Low cost high efficiency DC-DC converter for fuel cell powered auxiliary power unit of a heavy vehicle. IEEE Trans Power Electron 2006;21:587–91. https://doi.org/10.1109/TPEL.2006.872380.
[59] Mayyas AT, Ruth M, Pivovar B, Bender G, Wipke K. Manufacturing cost analysis for proton exchange membrane water electrolyzers. Golden, CO: National Renewable Energy Laboratory (NREL); 2019. Report No.: NREL/TP-6A20-72740. https://doi.org/10.2172/1557965.
[60] Ramasamy V, Zuboy J, Woodhouse M, O'Shaughnessy E, Feldman D, Desai J, et al. US solar photovoltaic system and energy storage cost benchmarks, with minimum sustainable price analysis: Q1 2023. Golden, CO: National Renewable Energy Laboratory (NREL); 2023. Report No.: NREL/TP-7A40-87303. https://doi.org/10.2172/2005540.
[61] Short W, Packey DJ, Holt T. A manual for the economic evaluation of energy efficiency and renewable energy technologies. Golden, CO: National Renewable Energy Laboratory (NREL); 1995. Report No.: NREL/TP-462-5173. https://doi.org/10.2172/35391.
[62] Grimm A, de Jong WA, Kramer GJ. Renewable hydrogen production: a techno-economic comparison of photoelectrochemical cells and photovoltaic-electrolysis. Int J Hydrog Energy 2020;45:22545–55. https://doi.org/10.1016/j.ijhydene.2020.06.092.
[63] KG 2022 [accessed 5 February 2026], https://h2.live/en/news.
[64] Campbell-Stanway C, Becerra V, Prabhu S, Bull J. Investigating the role of byproduct oxygen in UK-based future scenario models for green hydrogen electrolysis. Energies 2024;17:281. https://doi.org/10.3390/en17020281.
[65] Wei X, Sharma S, Waeber A, Wen D, Sampathkumar SN, Margni M, et al. Comparative life cycle analysis of electrolyzer technologies for hydrogen production: manufacturing and operations. Joule 2024;8:3347–72. https://doi.org/10.1016/j.joule.2024.09.007.
[66] Park J, Ryu KH, Kim CH, Cho WC, Kim M, Lee JH, et al. Green hydrogen to tackle the power curtailment: meteorological data-based capacity factor and techno-economic analysis. Appl Energy 2023;340:121016. https://doi.org/10.1016/j.apenergy.2023.121016.